Consistent dust and gas models for protoplanetary disks. II. Chemical networks and rates

Kamp, I.; Thi, W.-F.; Woitke, P.; Rab, C.; Bouma, S.; Ménard, F.

Published in:
Astronomy & astrophysics

DOI:
10.1051/0004-6361/201730388

Publication date:
2017

A&A 607, A41 (2017)
DOI: 10.1051/0004-6361/201730388

Astronomy & Astrophysics

Consistent dust and gas models for protoplanetary disks

II. Chemical networks and rates

I. Kamp[1], W.-F. Thi[2], P. Woitke[3], C. Rab[4], S. Bouma[1], and F. Ménard[5]

[1] Kapteyn Astronomical Institute, University of Groningen, Postbus 800, 9700 AV Groningen, The Netherlands
[2] Max Planck Institute for Extraterrestrial Physics, Giessenbachstrasse, 85741 Garching, Germany
[3] SUPA, School of Physics & Astronomy, University of St. Andrews, North Haugh, St. Andrews, KY16 9SS, UK
[4] University of Vienna, Department for Astrophysics, Türkenschanzstr.17, 1180 Vienna, Austria
[5] University of Grenoble Alpes, CNRS, IPAG, 38000 Grenoble, France

Received 3 January 2017 / Accepted 20 July 2017

ABSTRACT

Aims. We aim to define a small and large chemical network which can be used for the quantitative simultaneous analysis of molecular emission from the near-IR to the submm. We also aim to revise reactions of excited molecular hydrogen, which are not included in UMIST, to provide a homogeneous database for future applications.
Methods. We have used the thermo-chemical disk modeling code ProDiMo and a standard T Tauri disk model to evaluate the impact of various chemical networks, reaction rate databases and sets of adsorption energies on a large sample of chemical species and emerging line fluxes from the near-IR to the submm wavelength range.
Results. We find large differences in the masses and radial distribution of ice reservoirs when considering freeze-out on bare or polar ice coated grains. Most strongly the ammonia ice mass and the location of the snow line (water) change. As a consequence molecules associated to the ice lines such as N_2H^+ change their emitting region; none of the line fluxes in the sample considered here changes by more than 25% except CO isotopologues, CN and N_2H^+ lines. The three-body reaction N+H_2+M plays a key role in the formation of water in the outer disk. Besides that, differences between the UMIST 2006 and 2012 database change line fluxes in the sample considered here by less than a factor of two (a subset of low excitation CO and fine structure lines stays even within 25%); exceptions are OH, CN, HCN, HCO^+ and N_2H^+ lines. However, different networks such as OSU and KIDA 2011 lead to pronounced differences in the chemistry inside 100 au and thus affect emission lines from high excitation CO, OH and CN lines. H_2 is easily excited at the disk surface and state-to-state reactions enhance the abundance of CH^+ and to a lesser extent HCO^+. For sub-mm lines of HCN, N_2H^+ and HCO^+, a more complex larger network is recommended.
Conclusions. More work is required to consolidate data on key reactions leading to the formation of water, molecular ions such as HCO^+ and N_2H^+ as well as the nitrogen chemistry. This affects many of the key lines used in the interpretation of disk observations. Differential analysis of various disk models using the same chemical input data will be more robust than the interpretation of absolute fluxes.

Key words. astrochemistry – molecular data – protoplanetary disks – methods: numerical

1. Introduction

Observations often detect a multitude of simple molecules which have bright emission lines in protoplanetary disks such as CO, HCO^+, HCN, CN, N_2H^+, H_2CO, CH^+ (e.g., Thi et al. 2004; Dutrey et al. 2007; Öberg et al. 2010; Thi et al. 2011a; Qi et al. 2013a). Even though studying differences in the molecular content of disks is interesting in its own right, molecules are frequently used as tracers of disk properties, such as outer gas radius (e.g., Panić & Hogerheijde 2009), the position of the CO ice line (e.g., Qi et al. 2013b), the ionization degree (e.g., Qi et al. 2003), the irradiation by X-rays (e.g., Aikawa & Herbst 2001) and the deuterium fractionation (e.g., Ceccarelli et al. 2005).

Due to the importance of molecular lines for protoplanetary disk research, several studies have focussed on the size of chemical networks and the uncertainties in chemical rates. Semenov et al. (2004) find that the midplane and the ionized surface layer can be described using very small networks, while the intermediate layer, where most of the ion-molecule chemistry happens, requires large networks with of the order of 100 species. Vasyunin et al. (2004) varied the rate constants within the uncertainties using a Monte Carlo approach and conditions representative of diffuse and dark clouds. In dark clouds, they find abundance changes of less than 0.5 dex for simple species such as N_2H^+, HCO^+, while HCN can change up to 1 dex. Interestingly, CO is among the most robust species. Vasyunin et al. (2008) expanded this study to protoplanetary disk conditions. Again, CO is the most robust species while HCN, N_2H^+, and HCO^+ column densities can typically vary by a factor 2.5–3. Local changes can, however, be larger than this.

Thermo-chemical disk models often use a single network throughout the entire disk. When comparing such models to a set of observational data including molecular emission lines, we often rely in a first step on simple molecules such as CO and HCN. For those molecules, the chemistry is simple, resulting in robust model predictions. The chemical network used in this step should be small and fast to solve in order to allow the computation of larger model grids or the use of evolutionary search strategies to derive basic properties of the disk such as the dust mass, the mass of CO gas, radial extent of the disk,

and the amount of flaring. In a second step, based on the previously found disk model, species with a more complex chemistry can be studied using larger chemical networks. It is important however to note that the chemical network is only one aspect in the interpretation of line observations. The other one, which is not addressed in this work, is the calculation of the excitation of the molecule which can be limited by the availability of molecular data (mainly collision cross sections), the complexity of IR and UV pumping or resonance scattering for optically thick lines (e.g., Cernicharo et al. 2009; Bethell & Bergin 2011; Kamp et al. 2013; Thi et al. 2013).

We develop in this paper simple rules for the construction of chemical networks that avoid artificial sinks and ensure links between various sub-networks such as the carbon, oxygen and nitrogen chemistry. We use a standard T Tauri disk model from Woitke et al. (2016) to study the impact of the size of the network, different chemical databases and ice adsorption scenarios on the species mass and emission from a representative sample of atomic and molecular lines (Sect. 2). Woitke et al. (2016) show that time-dependent chemistry has little effect on the resulting line fluxes at ages beyond 0.5 Myr. Hence, we focus here entirely on stationary chemistry. In Sect. 3, we discuss how changes in the UMIST database and the use of other databases affect the disk chemistry and line emission (Sects. 3.2 and 3.3). We investigate the role of three-body reactions for water chemistry (Sect. 3.3) and how the composition of the grains (bare or polar ices) affects the various ices reservoirs and emission lines connected to them (Sect. 3.4). We study the importance of reactions with excited molecular hydrogen (Sect. 3.5) and we end with assessing which emission lines require the use of larger chemical networks (Sect. 3.6).

2. Modeling

2.1. The disk model

We chose for this study a parametrized disk structure representative of a typical T Tauri star. The full model is described in Woitke et al. (2016). Table 1 repeats only the most important stellar and disk parameters.

To calculate the two dimensional physical and chemical structure, we used the radiation thermo-chemical disk code ProDiMo (Woitke et al. 2009a; Kamp et al. 2010; Thi et al. 2011b). The disk structure was set up using a tapered edge and mildly flaring geometry ($\beta = 1.15$). It extends from 0.07 to 700 au (characteristic radius at 100 au) and contains a gas mass of 0.033 $M_\odot$. The dust grain opacities were calculated using hollow spheres and a mixture of 60% silicates and 15% amorphous carbon with 25% vacuum (Min et al. 2016b) and we use the canonical dust-to-gas mass ratio of 0.01.

Here we have used a model series where we vary the base set of reaction rates, the set of adsorption energies, and the size of the chemical network using stationary chemistry. The reaction rate databases are UMIST2012 (McElroy et al. 2013), UMIST2006 (Woodall et al. 2007), OSU (Ohio State University chemical network from Eric Herbst) and KIDA2011 (Wakelam et al. 2012). Three sets of adsorption energies are taken from Aikawa et al. (1996), Garrod & Herbst (2006), and UMIST2012 (McElroy et al. 2013). The adsorption energies will be discussed in more detail in Sect. 3.4. The rules for compiling the small and large chemical network are provided in the next subsection. Table 2 describes the entire model series.

Since the disk chemistry and heating and cooling balance are intimately coupled, we fixed the gas temperature structure to that of the reference model 1 (UMIST2012, adsorption energies from Aikawa et al. 1996). This has allowed us to interpret changes in the chemical structure and emitted line fluxes entirely from the various chemical input data sets. The coupling of heating and cooling and chemical equations is highly non-linear, so the impact of our approximation can only be checked from additional models. We calculated a single additional model where we used the KIDA database and re-computed the gas temperature self-consistently. Our models – discussed in more detail in the next section – show that KIDA produces less water compared to UMIST in the warm surface layer stretching to a few au at gas temperatures higher than 200 K. Indeed, the additional model shows that the gas temperature in that layer increases slightly since the water cooling is diminished with respect to the

Table 1. Basic model parameters for the standard T Tauri disk.

Quantity	Symbol	Value
Stellar mass	M_*	0.7 $M_\odot$
Effective temperature	$T_{\rm eff}$	4000 K
Stellar luminosity	L_*	1.0 $L_\odot$
FUV excess	$f_{\rm UV}$	0.01
	$p_{\rm UV}$	1.3
Cosmic ray ionization rate	$\zeta_{\rm CR}$	1.7×10^{-17} s^{-1}
Chemical heating efficiency	$\gamma^{\rm chem}$	0.2
Disk gas mass[1]	$M_{\rm gas}$	0.033 $M_\odot$
dust-to-gas mass ratio	δ	0.01
Inner disk radius	$R_{\rm in}$	0.07 au
Outer disk radius[2]	$R_{\rm out}$	700 au
Tapered edge radius	$R_{\rm taper}$	100 au
Radial column density power index	ϵ	1.0
Reference radius	R_0	100 au
Scale height at R_0	H_0	10.0 au
Disk flaring power index	β	1.15
Minimum dust particle radius	$a_{\rm min}$	0.05 μm
Maximum dust particle radius	$a_{\rm max}$	3000.0 μm
Dust size distribution power index	$a_{\rm pow}$	3.5

Notes. [(1)] The disk mass is a factor 3.3 higher than in the original Woitke et al. (2016) model. [(2)] The outer radius is defined as the radius where the surface density column drops to $N_{\langle {\rm H} \rangle, {\rm ver}} = 10^{20}$ cm^{-2}.

Table 2. Series of disk models.

Model	$E_{\rm ads}$	Network size, mode	Base rates
model 1	Aikawa	small, steady state	UMIST2012 + CL reactions
model 2	Aikawa	small, steady state	UMIST2006
model 3	Aikawa	small, steady state	OSU
model 4	Aikawa	small, steady state	KIDA2011
model 1a	Aikawa	small, steady state	UMIST2012
model 5	GH06	small, steady state	UMIST2012 + CL reactions
model 6	UMIST2012	small, steady state	UMIST2012 + CL reactions
model 7	T-dependent	small, steady state	UMIST2012 + CL reactions
model 8	UMIST2012	large, steady state	UMIST2012 + CL reactions

Notes. The columns denote the set of adsorption energies $E_{\rm ads}$, chemical network and rate database used.

Table 3. Selection of elements and chemical (gas+ice) species in the small network.

12 elements	H, He, C, N, O, Ne, Na, Mg, Si, S, Ar, Fe	
(H)	H, H^+, H^-, **H_2**, H_2^+, H_3^+, H_2^{exc}	7
(He)	He, He^+,	2
(C–H)	C, C^+, C^{++}, CH, CH^+, **CH_2**, CH_2^+, CH_3, CH_3^+, **CH_4**, CH_4^+, CH_5^+,	12
(C–N)	CN, CN^+, **HCN**, HCN^+, $HCNH^+$	5
(C–O)	**CO**, CO^+, HCO, HCO^+, **CO_2**, CO_2^+, HCO_2^+,	7
(N–H)	N, N^+, N^{++}, NH, NH^+, NH_2, NH_2^+, **NH_3**, NH_3^+, NH_4^+	9
(N–N)	**N_2**, N_2^+, HN_2^+,	3
(N–O)	NO, NO^+,	2
(O–H)	O, O^+, O^{++}, OH, OH^+, **H_2O**, H_2O^+, H_3O^+,	8
(O–O)	**O_2**, O_2^+,	2
(O–S)	SO, SO^+, **SO_2**, SO_2^+, HSO_2^+	5
(S–H)	S, S^+, S^{++},	3
(Si–H)	Si, Si^+, Si^{++}, SiH, SiH^+, SiH_2^+,	6
(Si–O)	**SiO**, SiO^+, $SiOH^+$,	3
(Na)	Na, Na^+, Na^{++},	3
(Mg)	Mg, Mg^+, Mg^{++},	3
(Fe)	Fe, Fe^+, Fe^{++},	3
(Ne)	Ne, Ne^+, Ne^{++},	3
(Ar)	Ar, Ar^+, Ar^{++},	3
ice	CO#, H_2O#, CO_2#, CH_4#, NH_3#, SiO#, SO_2#, O_2#, HCN#, N_2#	10
species	total	100

Notes. Neutral more stable molecules are indicated in bold font and ices are indicated by a trailing #.

UMIST reference model. However, the effects are very subtle, if the overall gas temperature distribution is considered.

2.2. The chemical network

We followed two approaches here: (1) provide a robust and fast standard that enables to deal with simple species (robust tracers) such as C, O, Ne, CO, CN, CO_2, OH, and H_2O; (2) provide a consistent standard that can be used as a starting point for further investigation of the chemistry of more complex species such as HCN, H_2C_2, HCO^+, N_2H^+. So far, in the literature no chemistry standard has been defined for disks in the context of multi-wavelength fitting of observational data. Instead many different species lists are used and we only start to understand the impact of the species choices and/or presence of ices and electron sinks for the abundance of specific low abundance tracers such as HCO^+ ($\epsilon \sim 10^{-10}$) (Kamp et al. 2013; Rab et al., in prep.).

Table 3 shows the selection used for many years in the disk modeling for the Herschel open time key program GASPS (Gas Evolution in Planetary Systems, PI: B. Dent); we subsequently refer to this as the small network. The abundances of the robust tracers listed above should be calculated with sufficient accuracy and this will be tested in Sect. 3.6.

Table 4 details the selection of chemical species in the large network. We cover the most important C/N/O chemistry and a simple S and Si chemistry. Other elements (Na, Mg, Fe, Ne, Ar) are represented only by their atoms and ions. Detailed PAH charging is used, as well as a large selection of ice species. The selection of species is largely based on the chemical networks of Prasad & Huntress (1980; C−H, C−C chemistry), van Dishoeck (1990; C−H chemistry) Sternberg & Dalgarno (1995; Si-chemistry, S−H chemistry, N-chemistry, O−H chemistry), Agúndez et al. (2008; high temperature C−H, C−C chemistry), Hily-Blant et al. (2013; N-chemistry). The size of our network is controlled by a combination of species becoming less reactive or saturated. We apply the following rules to ensure the completeness of the chemical network used:

- Negative ions/molecules have been omitted for the time being except H^-.
- We include for all atoms/molecules the positively charged counterpart (for elements also double charged). In some cases (HeH, HNS, HSO, CH_3O), the neutral one is missing since it is not present/has no reactions in UMIST (e.g., unstable molecule or other reasons).
- C−H chemistry processes via H_2 addition reactions up to CH_5^+, which is the maximum hydrogenation possible. CH_5^+ can then recombine dissociatively to give the closed-shell molecule CH_4. We proceed similarly for Si-H chemistry, thus stopping at SiH_5^+, and for O-H chemistry, thus stopping at H_3O^+.
- We identify the neutral more stable species to be H_2, CH_2, CH_4, C_2, C_3, C_4, C_2H_2 (acetylene), C_2H_4 (ethylene), C_3H_2 (cyclopropenylidene), HCN (hydrogen cyanide), CO, CO_2, H_2CO (formaldehyde), CH_3OH (methanol), CS (carbon monosulfide), H_2CS (thioformaldehyde), NH_3 (ammonia), NO_2, HNO (nitroxyl), N_2, H_2O, SO_2, H_2S (hydrogen sulfide), OCS (carbonyl sulfide), O_2, SiH_4 (silane), SiC (silicon carbide), SiN (silicon nitride), SiO (silicon monoxide), SiS (silicon sulfide). For those molecules, we ensure that the respective positive ion and the protonated ion are included. The exception is HNO_2^+, which is not included in UMIST (HNO_2 is included as species in UMIST, but has no reactions).
- We decided to keep the isomers CH_3O and CH_2OH to study the gas phase formation of methanol. We also keep the isomers HNC and HCN since they are both observed. However, we only include the ion HCN^+ and subsequent hydrogenation.
- We included several species that link the chemical networks with each other, especially for the heavier elements such

Table 4. Selection of elements and chemical (gas+ice) species in the large network.

13 elements	H, He, C, N, O, Ne, Na, Mg, Si, S, Ar, Fe, PAH	
(H)	H, H^+, H^-, **H_2**, H_2^+, H_3^+, H_2^{exc}	7
(He)	He, He^+,	2
(He–H)	HeH^+,	1
(C−H)	C, C^+, C^{++}, CH, CH^+, CH_2, CH_2^+, CH_3, CH_3^+, **CH_4**, CH_4^+, CH_5^+,	12
(C−C)	**C_2**, C_2^+, C_2H, C_2H^+, **C_2H_2**, $C_2H_2^+$, C_2H_3, $C_2H_3^+$, **C_2H_4**, $C_2H_4^+$, C_2H_5, $C_2H_5^+$, **C_3**, C_3^+, C_3H, C_3H^+, **C_3H_2**, $C_3H_2^+$, $C_3H_3^+$, **C_4**, C_4^+, C_4H^+,	23
(C–N)	CN, CN^+, **HCN**, HCN^+, $HCNH^+$, HNC, H_2CN, OCN, OCN^+,	9
(C–O)	**CO**, CO^+, HCO, HCO^+, **CO_2**, CO_2^+, HCO_2^+, C_2O, C_2O^+, HC_2O^+, **H_2CO**, H_2CO^+, CH_3O, H_3CO^+, CH_2OH, **CH_3OH**, CH_3OH^+, $CH_3OH_2^+$,	18
(C–S)	**CS**, CS^+, HCS, HCS^+, **H_2CS**, H_2CS^+, H_3CS^+, **OCS**, OCS^+, $HOCS^+$,	10
(N–H)	N, N^+, N^{++}, NH, NH^+, NH_2, NH_2^+, **NH_3**, NH_3^+, NH_4^+,	10
(N–N)	**N_2**, N_2^+, HN_2^+,	3
(N–O)	NO, NO^+, **NO_2**, NO_2^+, **HNO**, HNO^+, H_2NO^+,	7
(N–S)	NS, NS^+, HNS^+	3
(O–H)	O, O^+, O^{++}, OH, OH^+, **H_2O**, H_2O^+, H_3O^+,	8
(O–O)	**O_2**, O_2^+, O_2H^+,	3
(O–S)	SO, SO^+, **SO_2**, SO_2^+, HSO_2^+,	5
(S–H)	S, S^+, S^{++}, HS, HS^+, **H_2S**, H_2S^+, H_3S^+,	8
(Si–H)	Si, Si^+, Si^{++}, SiH, SiH^+, SiH_2, SiH_2^+, SiH_3, SiH_3^+, **SiH_4**, SiH_4^+, SiH_5^+,	12
(Si–C)	**SiC**, SiC^+, $HCSi^+$,	3
(Si–N)	**SiN**, SiN^+, $HNSi^+$,	3
(Si–O)	**SiO**, SiO^+, $SiOH^+$,	3
(Si–S)	**SiS**, SiS^+, $HSiS^+$,	3
(Na)	Na, Na^+, Na^{++},	3
(Mg)	Mg, Mg^+, Mg^{++},	3
(Fe)	Fe, Fe^+, Fe^{++},	3
(Ne)	Ne, Ne^+, Ne^{++},	3
(Ar)	Ar, Ar^+, Ar^{++},	3
(PAH)	PAH-, PAH, PAH^+, PAH^{++}, PAH^{+++},	5
ice	all neutral gas species except noble gases have ice counterparts	64
species	total	235

Notes. Neutral more stable molecules are indicated in bold font.

as S, N, and Si. An interesting example is the radical H_2CN (amidogen). It is formed by collisions between N and C−H chains and forms a CN bond. This connects the C−H, C−C chemistry with the nitrogen chemistry.

– Neutral atoms/molecules (including radicals) except noble gases can freeze out.

2.3. Reaction rates

ProDiMo selects from the UMIST2012 database all reactions among the species defined in the chemical network above. However, in some cases, we add additional reactions and/or overwrite UMIST reactions following the procedures described in Appendices A.1–A.7. Alternatively, we also use the UMIST2006, the OSU and the KIDA 2011 databases.

2.4. Element abundances

Table 5 describes the selection of elements and their respective abundances. These are very similar to the low-metal abundances used in the literature for example those of Lee et al. (1998). All following models adopt these low metal abundances.

Table 5. Elements, their abundances on the scale $\log n_H = 12$ and their masses in amu.

Element	$12 + \log \epsilon$	m [amu]	Element	$12 + \log \epsilon$	m [amu]
H	12.00	1.0079	Na	3.36	22.990
He	10.98	4.0026	Mg	4.03	24.305
C	8.14	12.011	Si	4.24	28.086
N	7.90	14.007	S	5.27	32.066
O	8.48	15.999	Ar	6.08	39.948
Ne	7.95	20.180	Fe	3.24	55.845

2.5. The line list

Table 6 describes the list of lines used to analize how changes in disk chemistry propagate into observable line fluxes. The atomic and molecular data is collected from LAMDA (Schöier et al. 2005), NIST and CHIANTI (Dere et al. 1997). Line fluxes are calculated using level populations from statistical equilibrium and a simplified 2D escape probability approach. Detailed radiative transfer tests show that line fluxes from escape probability are typically off by less than 50% except for close to edge on disk geometries and/or lines where a significant fraction of total emission originates from the inner rim (e.g., Woitke et al. 2009b; Antonellini et al. 2015).

Table 6. Lines used to analize flux changes related to chemistry.

Species	Designation	E_{up} [K]	A_{ij} [s^{-1}]	λ [μm]
CO	J = 2–1	16.60	6.910(–7)	1300.40
^{13}CO	J = 2–1	15.87	6.038(–7)	1360.23
C^{18}O	J = 2–1	15.81	6.011(–7)	1365.42
CO	J = 3–2	33.19	2.497(–6)	866.96
^{13}CO	J = 3–2	31.73	2.181(–6)	906.84
C^{18}O	J = 3–2	31.61	2.172(–6)	910.31
CO	J = 18–17	944.97	5.695(–4)	144.78
CO	J = 36–35	3668.78	3.638(–3)	72.84
CO	v = 1–0 J = 3–4	3116.70	1.950(1)	4.699950
CO	v = 1–0 J = 35–36	6523.52	1.407(1)	5.040484
CO	v = 2–1 J = 3–4	6162.10	3.745(1)	4.758863
OI	^{3}P$_1$–^{3}P$_2$	227.712	8.91(–5)	63.18
OI	^{3}P$_0$–^{3}P$_1$	326.579	1.750(–5)	145.53
OI	^{1}D$_2$–^{3}P$_2$	22 830.18	6.535(–3)	0.63003
CII	^{2}P$_{3/2}$–^{2}P$_{1/2}$	91.21	2.300(–6)	157.74
CI	^{3}P$_1$–^{3}P$_0$	23.620	7.880(–8)	609.14
CI	^{3}P$_2$–^{3}P$_1$	62.462	2.650(–7)	370.42
NeII	^{2}P$_{1/2}$–^{3}P$_{3/2}$	1122	8.59(–3)	12.815
NeIII	^{3}P$_1$–^{3}P$_2$	924.98	5.97(–3)	15.555
SII	^{2}D$_{5/2}$–^{4}S$_{3/2}$	21420	3.338(–4)	0.67164
SIII	^{3}P$_2$–^{3}P$_1$	1199.904	2.07(–3)	18.716
ArII	^{2}P$_{1/2}$–^{2}P$_{3/2}$	2059.72	5.3(–2)	6.985
ArIII	^{3}P$_0$–^{3}P$_1$	2259.2	5.19(–3)	21.816
FeII	^{6}D$_{9/2}$–^{6}D$_{7/2}$	553.6	2.13(–3)	25.988
SiII	^{2}P$_{1/2}$–^{2}P$_{3/2}$	413.21	2.132(–4)	34.807
OH	$^2\Pi_{1/2}$ 7/2$^+$–5/2$^-$	617.9	1.012	71.22
OH	$^2\Pi_{1/2}$ 7/2$^-$–5/2$^+$	617.6	1.014	71.17
OH	$^2\Pi_{1/2}$ 1/2$^-$–$^2\Pi_{3/2}$ 3/2$^+$	181.9	3.606(–2)	79.11
OH	$^2\Pi_{1/2}$ 1/2$^+$–$^2\Pi_{3/2}$ 3/2$^-$	181.7	3.598(–2)	79.18
OH	$^2\Pi_{3/2}$ 5/2$^-$–3/2$^+$	120.7	1.388(–1)	119.23
OH	$^2\Pi_{3/2}$ 5/2$^+$–3/2$^-$	120.5	1.380(–1)	119.44
o-H$_2$O	1_{10}–1_{01}	61.0	3.458(–3)	538.29
o-H$_2$O	2_{12}–1_{01}	114.4	5.593(–2)	179.53
o-H$_2$O	4_{23}–3_{12}	432.2	4.838(–1)	78.74
o-H$_2$O	8_{18}–7_{07}	1070.7	1.751	63.32
p-H$_2$O	1_{11}–0_{00}	53.4	1.842(–2)	269.27
p-H$_2$O	4_{13}–4_{04}	396.4	3.726(–2)	187.110
p-H$_2$O	3_{22}–2_{11}	296.8	3.524(–1)	89.988
o-H$_2$	v = 0–0 S(1) J = 3–1	1015	4.76(–10)	17.034
p-H$_2$	v = 0–0 S(2) J = 4–2	1682	2.754(–9)	12.278
p-H$_2$	v = 0–0 S(4) J = 6–4	3474	2.642(–8)	8.025
o-H$_2$	v = 0–0 S(9) J = 11–9	10262	4.898(–7)	4.694
o-H$_2$	v = 2–1 S(1) J = 3–1	12550	4.977(–7)	2.248
p-H$_2$	v = 1–0 S(0) J = 2–0	6472	2.526(–7)	2.223
o-H$_2$	v = 1–0 S(1) J = 3–1	6952	3.471(–7)	2.122
CN	N = 2–1 J = 5/2–3/2	16.34	1.143(–4)	1321.380
CN	N = 5–4 J = 11/2–9/2	81.64	2.027(–3)	528.78
HCN	J = 3–2	25.52	8.3559(–4)	1127.521
HCN	J = 4–3	42.53	2.054(–3)	845.66
CH$^+$	J = 2–1	120.195	4.760(–2)	179.594
CH$^+$	J = 4–3	400.086	0.3781	90.011
CH$^+$	J = 5–4	599.524	0.7346	72.137
HCO$^+$	J = 1–0	4.28	4.2512(–5)	3361.334
HCO$^+$	J = 3–2	25.68	1.4757(–3)	1120.478
HCO$^+$	J = 4–3	42.80	3.6269(–3)	840.380
N$_2$H$^+$	J = 3–2	26.83	1.2586(–3)	1072.558

Notes. The notation $x(-y)$ stands for $x\,10^{-y}$.

Details on collision cross sections and collision partners can be found in a series of papers: atoms, ions and H_2 (Woitke et al. 2009a), CH^+ (Thi et al. 2011a), double-ionized species (Aresu et al. 2012), CO (Thi et al. 2013), H_2O (Kamp et al. 2013). The collision data for the remaining molecules is taken from the LAMDA database. The CN collision partners are He and e; the HCO^+ collision partner is H_2; the HCN collision partners are H_2, He and e; the OH collision partners are ortho- and para-H_2.

3. Results

3.1. The base model

The physical properties of the reference model are described in detail in Woitke et al. (2016) and we summarize here a few key features relevant for the chemical studies. The model reaches total hydrogen number densities of 10^{14}–10^{16} cm^3 in the midplane inside 1 au. The dust temperature decreases from ~1500 K at the inner rim to 100 K at ~1 au. Gas and dust are thermally well coupled below $A_V \sim 1$ (toward the disk midplane). At the disk surface above $A_V = 1$, the gas temperature reaches values up to several 1000 K. Only in the outer disk atmosphere beyond 100 au and below $z/r = 0.4$ (corresponding to ~20° opening angle), the gas temperature drops below that of the dust.

The abundance distribution – using the small network – for the key species CO, CO#, CO_2, CO_2#, HCO^+, OH, H_2O#, CN, HCN, HCN#, NH_3, NH_3# is shown in Fig. 1 for the reference model (model1; note that the trailing # denotes the ice form of this species). The CO surface is reasonably well described using the PDR parameter $\log\chi/\langle n_H\rangle$. For values larger than −3.5, CO is efficiently photo dissociated[1] and has abundances below $\log n_{CO}/\langle n_H\rangle = \log\epsilon_{CO} = -8$. Here, $\langle n_H\rangle$ is the total hydrogen number density. The CO ice line is reasonably well described by the $T_{dust} = 20$ K line, but a rate equilibrium approach works even better (Antonellini 2016, white dashed line). The disk shows a ring of high CO_2 abundance inside 1 au. The CO_2 ice is sandwiched between the water and CO ice reservoirs. HCO^+ only resides in a very thin layer below the C^+/C/CO transition when the small chemical network is used.

The OH molecule constitutes the first step in the neutral-neutral chemical pathway to water formation. It is concentrated in the surface layers of the inner disk ($r < 10$ au) where gas temperatures are between 200 and 2000 K. Just below the OH reservoir, inside 0.5 au, densities are high enough to efficiently form water with an abundance of 10^{-4}. Beyond the snow line, water freezes out onto the cold dust grains. The water ice reservoir is outlined well by a rate equilibrium approach (Antonellini 2016, yellow dashed line) or using the water vapor pressure together with the local radiation field (Min et al. 2016a, white dashed line).

The disk model contains only minute amounts of CN in the disk atmosphere ($\log\epsilon_{CN} < -8$). Instead we identify two large HCN reservoirs with $\log\epsilon_{HCN} \sim -4$, a narrow ring around 0.2 au and a broader ring between 1 and 5 au. These two reservoirs sit below the $A_V = 1$ surface where $T_{gas} = T_{dust}$. An additional lower abundance reservoir ($\log\epsilon_{HCN} \sim -8$) can be found in the outer disk atmosphere beyond 100 au. The most stable nitrogen bearing molecule, NH_3 is only found in a very narrow ring close to the inner rim of the disk. In this particular model, NH_3 ice plays a minor role as a nitrogen reservoir.

Some of these results will depend on the details of the chosen disk model, on the set of adsorption energies used and also on the size of the chemical network. The impact of the latter two will be discussed in the subsequent sections.

[1] Self-shielding is taken into account using the approach described in Woitke et al. (2009a).

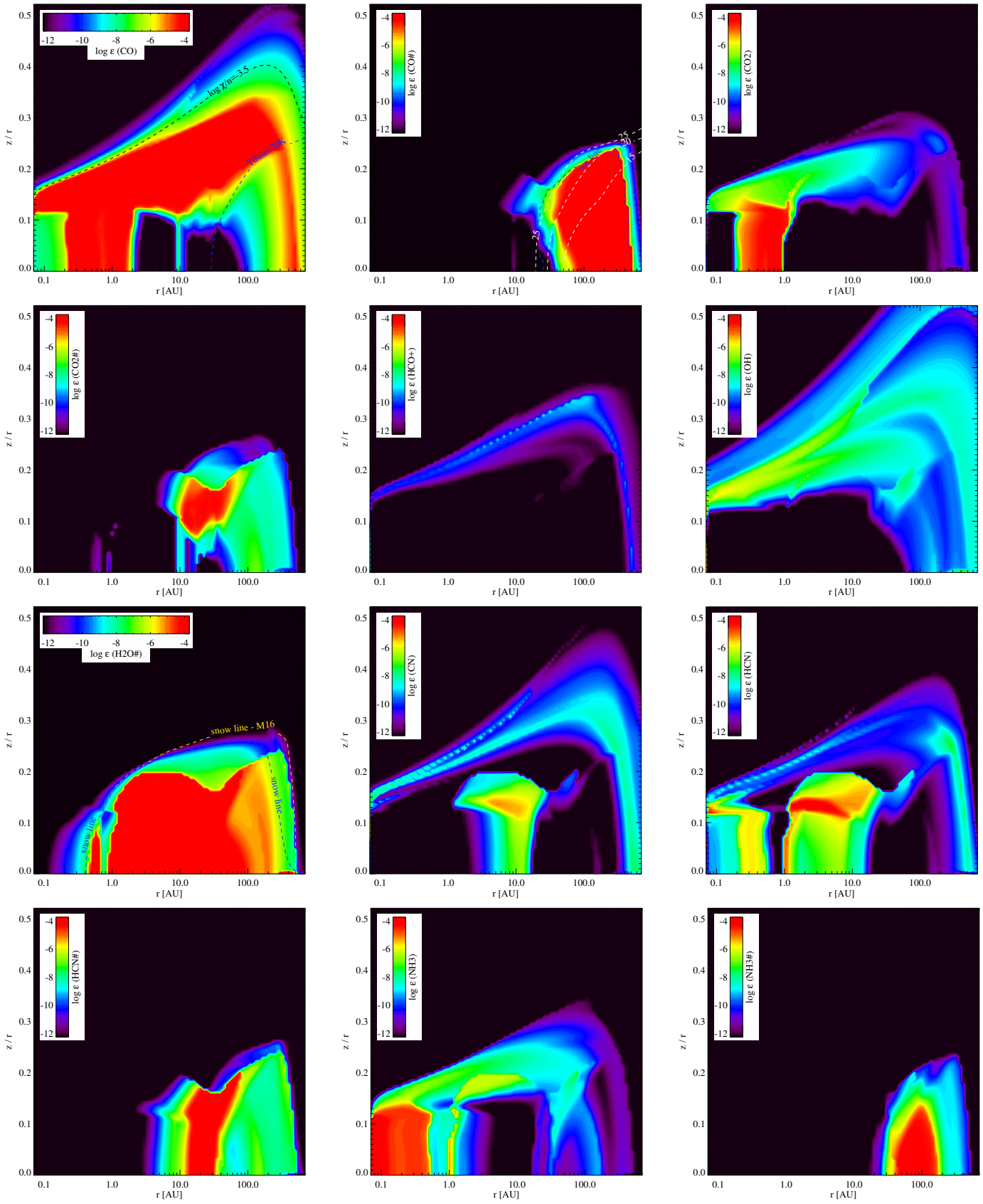

Fig. 1. Distribution of key species abundances in the base model: CO, CO#, CO_2, CO_2#, HCO^+, OH, H_2O#, CN, HCN, HCN#, NH_3, NH_3#. For CO, the black contour shows the PDR parameter $\log \chi/\langle n_H \rangle = -3.5$ and the blue contour $T_{dust} = 20$ K where CO starts to freeze out on dust grains. For CO#, the white dashed contours show dust temperatures of 15, 20 and 25 K and the blue dashed line shows the CO ice line estimate from rate equilibrium (Antonellini 2016). For water ice, two approximations of the snow line are indicated: (1) estimate based on the local density, dust temperature and radiation field (Min et al. 2016a, yellow dashed) and (2) estimate from rate equilibrium (Antonellini 2016, blue dashed).

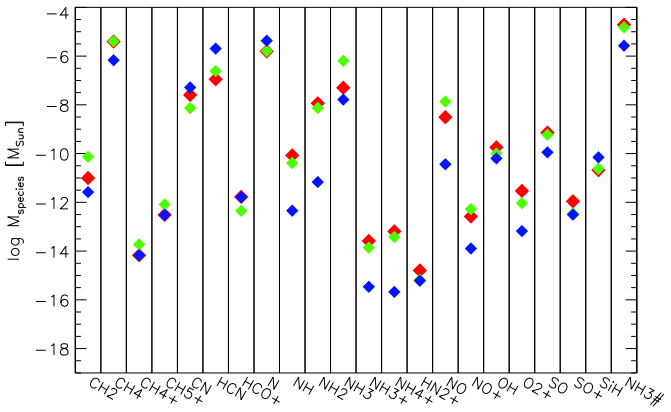

Fig. 2. Differences in species masses between three different sets of reactions: UMIST2012 plus collider reactions from UMIST2006 (red, model 1), UMIST2006 (green, model 2) and UMIST2012 (blue, model 1a).

3.2. Chemical rates from UMIST2006 to 2012

The revision of the UMIST database in 2012 reveals major differences in species masses especially for nitrogen bearing species. The main reason is the missing collider reactions with respect to the UMIST2006 rate file. Figure 2 shows this effect for the species that change by more than a factor three and have absolute masses above 10^{-15} $M_\odot$. Species not shown here vary by less than a factor three.

In the case of UMIST2012 without the collider reactions, water and OH abundances in the surface of the outer disk change by orders of magnitude; in fact, the entire water vapor reservoir on top of the water ice reservoir disappears (Fig. 3). This is also reflected in the water and OH line fluxes changing by a factor 3–10 (Fig. 4). The rates were not deliberately omitted, but simply not re-assessed in UMIST2012, hence the UMIST2006 collider reactions should be used (Millar, priv. comm.). Adding the collider reactions brings back the water and OH reservoir and also leads to a match of the water and OH line fluxes to within a factor of 2–3 (Fig. 5). The three-body (collider) reaction opening the water formation pathway is

$$\mathrm{N + H_2 + M \rightarrow NH_2}, \quad (1)$$

with a reaction rate of 10^{-26} cm^6 s^{-1} (Avramenko & Krasnenkov 1966). The rate is constant over the temperature range 564−796 K according to NIST. Since we extrapolate rates outside the temperature range, it gets applied also in the somewhat cooler disk surface regions (20−300 K). This rate stems from a very old measurement and definitely needs to be revisited. NH_2 subsequently reacts with oxygen to form NH and OH. Both radicals react further to form water (Kamp et al. 2013). The more classical neutral-neutral pathway identified for example by Glassgold et al. (2009)

$$\mathrm{O \xrightarrow{H_2} OH \longrightarrow H_2H_2O} \quad (2)$$

acts at higher gas temperatures ($T_{\rm gas} \gg 200$ K) closer to the star.

CN, OH and HCO^+ show differences in species mass of up to 0.5 dex between UMIST2006 and UMIST2012 (plus collider reactions). Lines of these species are frequently observed in the far-IR and submm wavelength range and their predicted line fluxes can differ by up to a factor 2.5 for CN and OH and up to a factor six for HCO^+, with UMIST2012 giving systematically higher fluxes (Fig. 5). Throughout the remainder of this paper, we use "UMIST2012" as a replacement for "UMIST2012 rate database including the collider reactions".

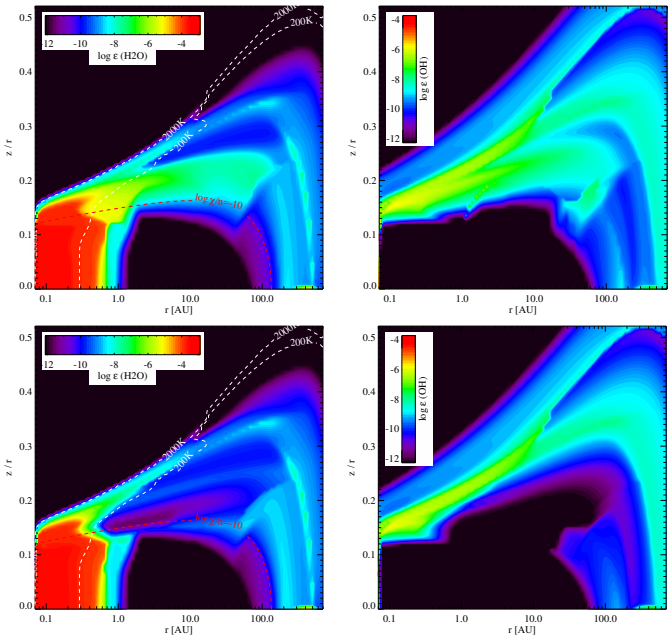

Fig. 3. Comparison of water and OH abundances in the UMIST2012 model with (*top*, model 1) and without collider reactions (*bottom*, model 1a).

3.3. Chemical reaction databases

We test the impact of different sets of reaction rates on the overall disk chemistry and appearance. Three databases are investigated: UMIST2012 (model 1), OSU (model 3) and KIDA (model 4). In all cases, we use the small chemical network and the adsorption energies of Aikawa et al. (1996). We also keep the physical and thermal structure of the underlying disk constant.

Given that these databases have been compiled with different focus, it is not surprizing that almost one third of the species masses change by more than 0.5 dex. In addition, collider reactions are not a priori included in these databases; hence water and OH are affected in the same way as described in Sect. 3.2. Figure 6 provides an overview of a few key species for OSU and KIDA and can be compared to Figs. 1 and 3.

However, despite these large changes in the overall chemical structure, some line tracers stay very robust while others change by more than 1 dex (see Figs. 7 and 8):

– The low excitation CO lines hardly change. This is due to the simple molecular cloud like chemistry in the outer disk. However, there are significant changes in the high excitation rotational lines and ro-vibrational lines that originate in the inner 10 au where CO chemistry is driven by ion-molecule and in lower layers by neutral-neutral reactions. Interestingly, OSU gives systematically higher fluxes, while KIDA is lower than UMIST2012. This relates to the depth at which the C^+/C/CO transition is reached in those different networks. Self-shielding is treated in the same way for all three networks. The main CO formation reactions are via OH producing CO^+. The OH radical can react with H_2, N or C^+ and the latter forms CO^+ (OH + $C^+ \rightarrow CO^+ + H$). Subsequent reactions with H and H_2 lead to CO ($CO^+ + H \rightarrow CO + H^+$ and $CO^+ + H_2 \rightarrow HCO^+ + H$ followed by $HCO^+ + e \rightarrow CO + H$). Reaction rates for these differ between the networks. Apparently, even small rate differences can lead to significant differences in line fluxes. The transition lies

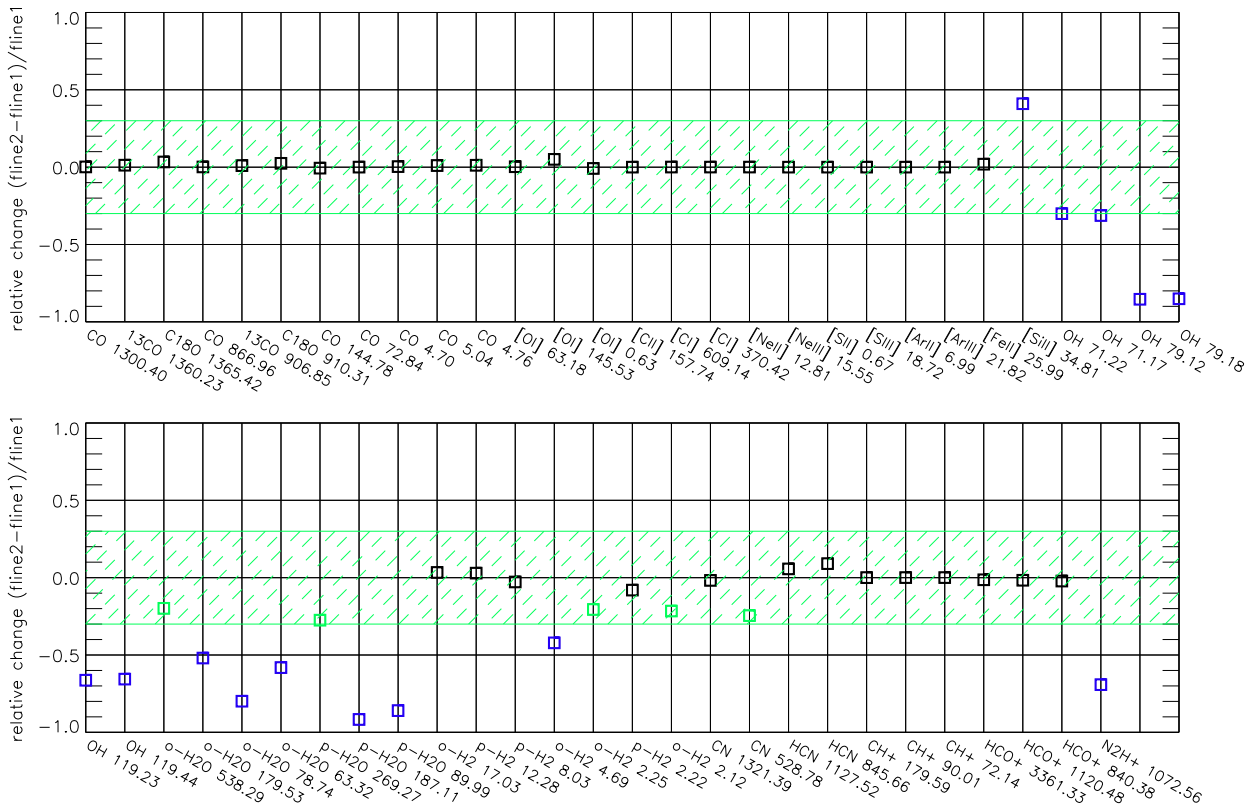

Fig. 4. Comparison of line fluxes for two sets of reactions: UMIST2012 plus CL reactions from UMIST2006 (fline1, model 1) and UMIST2012 (fline2, model 1a). Black and green squares denote differences of less than 25% and less than a factor two respectively, blue squares and red triangles denote differences larger than a factor three and ten respectively.

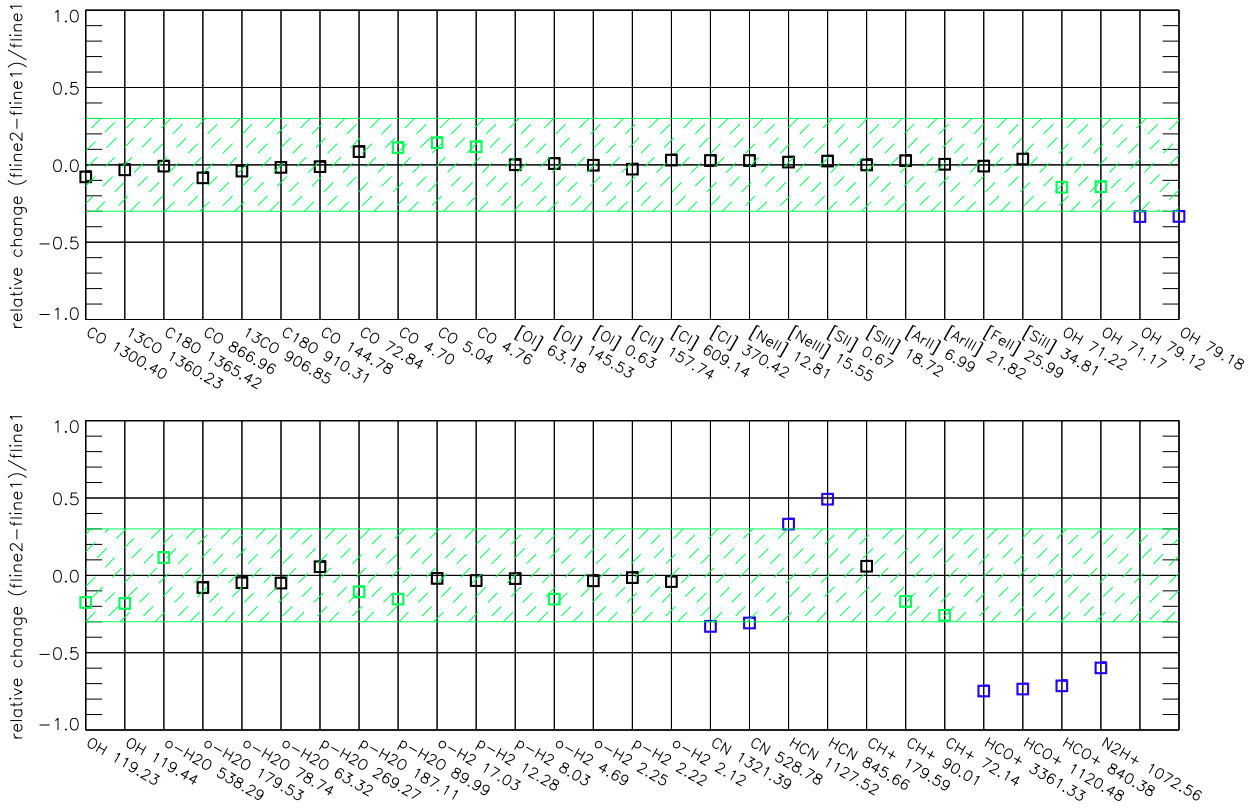

Fig. 5. Comparison of line fluxes for two sets of reactions: UMIST2012 plus CL reactions from UMIST2006 (fline1, model 1) and UMIST2006 (fline2, model 2). Black and green squares denote differences of less than 25% and less than a factor two respectively, blue squares and red triangles denote differences larger than a factor three and ten respectively.

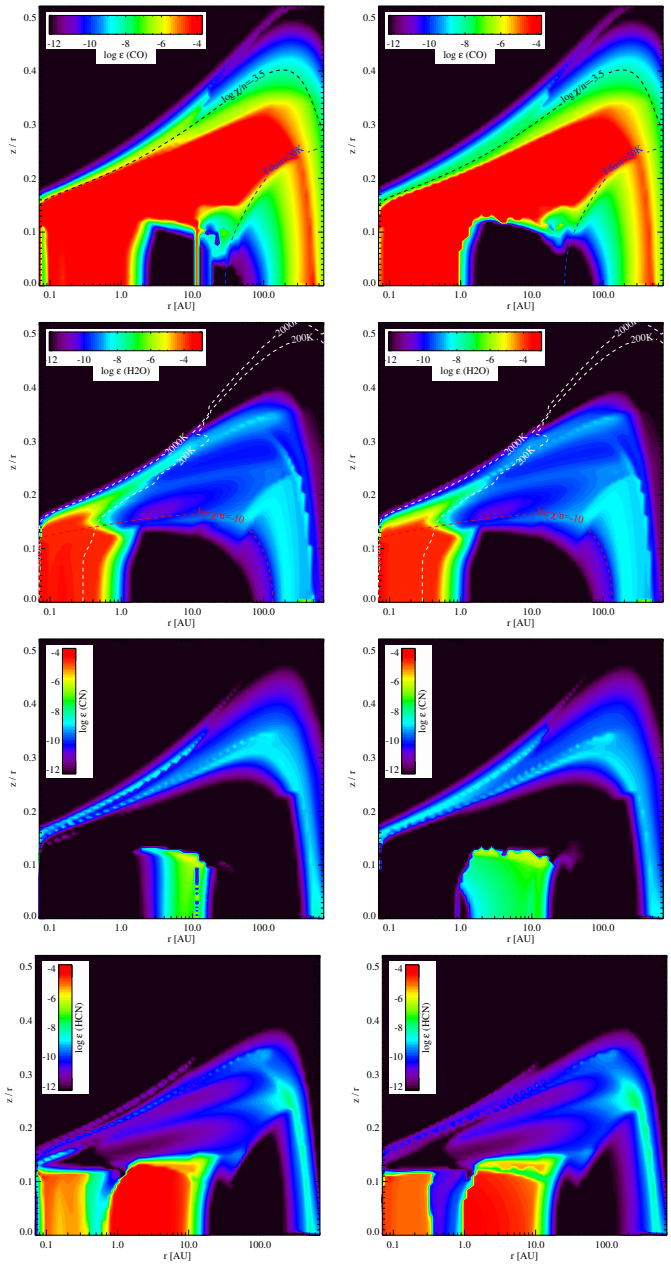

Fig. 6. Distribution of key species abundances using OSU (*left*) and KIDA (*right*): CO, H_2O, CN, HCN. Contours are the same as those in Figs. 1 and 3.

closest to the surface in the OSU model, while it lies deepest in the KIDA model (see Figs. 1 and 6); note that the CO high excitation lines react very strongly to changes in temperature and the C^+/C/CO transition has a steep vertical temperature gradient.

– The neutral and ionized atomic line fluxes are very robust and stay within a factor two across all networks; those species are dominated by photochemistry and their abundance (and line flux) directly reflects the choice of elemental abundances.
– H_2 chemistry is driven by formation on dust and photodissociation; these processes are implemented outside the specific network. A crucial reaction in the inner disk destroying H_2 is collisions with atomic oxygen, leading to the formation of OH. The rate constants do not differ much in the three networks
  UMIST – $A = 3.14 \times 10^{-13}$, $B = 2.7$, $C = 3150$ (297–3532 K);
  OSU – $A = 3.44 \times 10^{-13}$, $B = 2.67$, $C = 3160$ (1–40 000 K);
  KIDA – $A = 3.44 \times 10^{-13}$, $B = 2.67$, $C = 3160$ (10–280 K).
  However, for the reactions consuming OH, the rate coefficients are different in the three networks, propagating into the OH abundances in the surface layers inside 10 au. Emission lines of molecular hydrogen turn out to be mostly within a factor of three. Many of the H_2 lines discussed here originate in a thin surface layer limited in depth by the dust continuum. The high rotational line at 4.694 μm as well as the rovibrational lines are optically thin similar to what was found by Nomura & Millar (2005). This makes line flux predictions very sensitive to the exact placement of the H/H_2 transition in the disk model.
– HCN lines originating in the outer disk are also very robust; again, similar to the CO case, the chemistry here is largely molecular cloud chemistry.
– CN outer disk abundances are lower in the OSU and KIDA disk models (see Figs. 1 and 6) and the corresponding lines originating in the outer disk are systematically weaker for those networks compared to UMIST2012. One difference in the networks is the CN destruction reaction with oxygen, which is a factor of approximately two stronger in OSU and KIDA at low temperatures compared to UMIST2012.
– OH and water lines differ within a factor ten between the OSU/KIDA and UMIST2012. This is mainly due to the missing collider reactions that affect the outer lower reservoirs of these two molecules.
– The largest differences (more than one order of magnitude) are seen in line fluxes of CH^+ between UMIST2012 and KIDA. This is due to differences in reaction rates leading to the formation and destruction of this radical (see Table 7).

Table 7. Comparison of rate coefficients for CH^+ formation and destruction reactions.

Reaction	KIDA 2011			UMIST 2012		
	A	*B*	*C*	*A*	*B*	*C*
$C + H_3^+$	2(–9)	0.0	0.0	2.00(–9)	0.0	0.0
$C^+ + H_2$	7.8(–10)	0.0	4540.0	1.00(–10)	0.0	4640.0
$CH^+ + H_2$	1.20(–9)	0.0	0.0	1.20(–9)	0.0	0.0
$CH^+ + e$	7(–8)	–0.5	0.0	1.50(–7)	–0.42	0.0

Notes. The coefficients *A*, *B* and *C* have their usual meaning (see e.g., McElroy et al. 2013). The notation $x(-y)$ denotes $x\,10^{-y}$.

3.4. Adsorption energies

After having seen differences arizing from different networks, we focus now on adsorption energies that affect the gas/ice reservoirs in the disk. Collings et al. (2004) found for example that CO can be trapped in the polar water ice at much higher temperatures than in a non-polar CO ice. The dependence of chemical abundances on the specific grain surface – SiO_2, polar, non-polar – has already been noted by Bergin et al. (1995). Here, we explore systematically the effects of using different sets of adsorption energies and explore a first simple model that illustrates the effect of surface dependent adsorption energies.

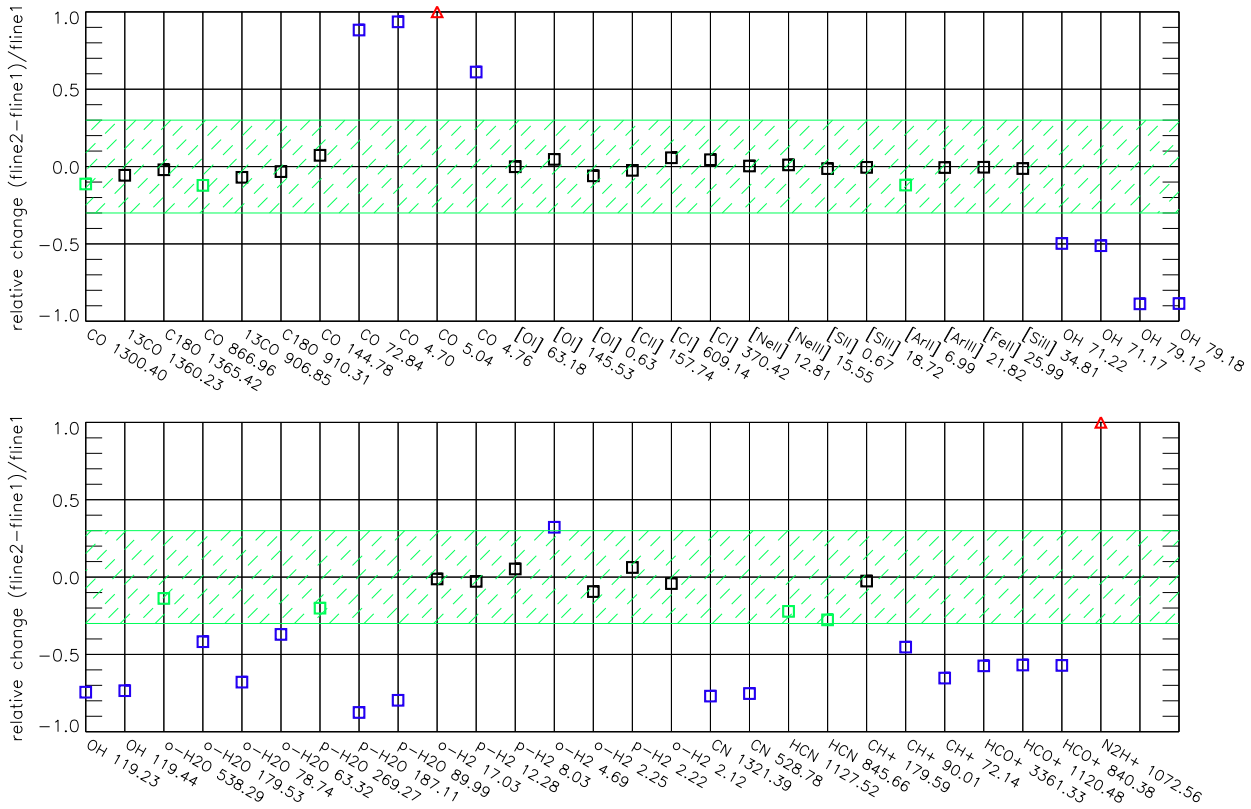

Fig. 7. Comparison of line fluxes for two databases: UMIST2012 (fline1, model 1) and OSU (fline2, model 3). Black and green squares denote differences of less than 25% and less than a factor two respectively, blue squares and red triangles denote differences larger than a factor three and ten respectively.

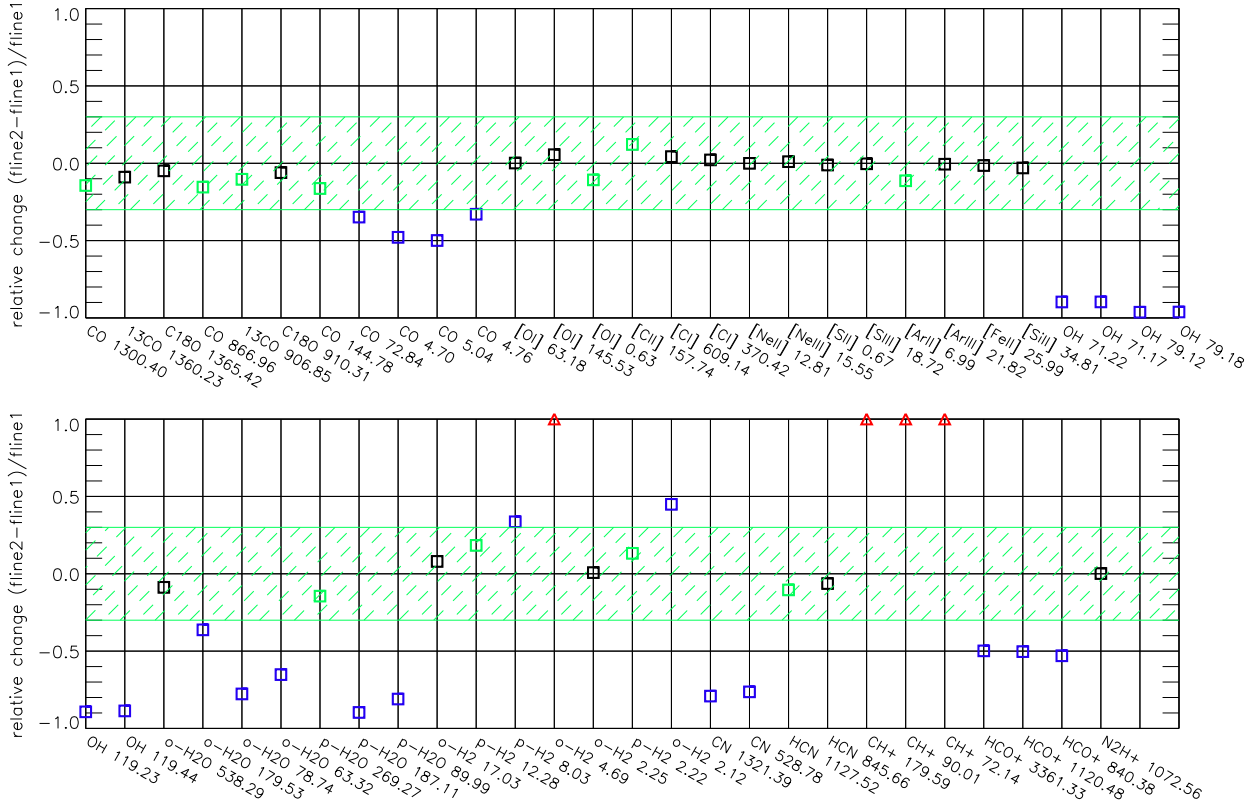

Fig. 8. Comparison of line fluxes for two databases: UMIST2012 (fline1, model 1) and KIDA (fline2, model 4). Black and green squares denote differences of less than 25% and less than a factor two respectively, blue squares and red triangles denote differences larger than a factor three and ten respectively.

The thermal desorption rate of a species i depends among other variables also on the adsorption energy $E_{\rm ads}(i)$ (expressed in K)

$$R = n_{i\#}\nu_{\rm osc}(i)\exp\left(-\frac{E_{\rm ads}(i)}{T_{\rm dust}}\right)\ {\rm cm^{-3}\ s^{-1}}, \quad (3)$$

where $\nu_{\rm osc}(i)$ is the oscillation frequency of species i, $n_{i\#}$ the density of desorbable species i on the grain surface[2], and $T_{\rm dust}$ the temperature of the grain. The oscillation frequency depends only weakly on the adsorption energy of the species, thus making the exponential term in Eq. (3) the dominant one.

Adsorption energies measured in experiments differ largely depending on whether they are measured from ice on top of the same ice, ice mixtures or ice on bare graphite or silicate grains. Figure 9 shows two examples for values collected for NH_3 and HCN ice. The set of adsorption energies from Aikawa et al. (1996) corresponds to bare carbonaceous or silicate surfaces. Alternatively, Garrod & Herbst (2006) compiled a set of adsorption energies that is valid for non-porous water ice surfaces. Figure 9 shows that most values found in the literature indeed group around either the low bare grain value or the higher value on water ice. Values for the adsorption of a species on its own ice reside somewhere in between (see e.g., NH_3 vapor enthalpy and NH_3 on ammonia ice, Sandford & Allamandola 1993). UMIST2012 recommends a set of adsorption energies that largely agrees (within 30%) with Garrod & Herbst (2006). The only exception among the species in common is $HCOOCH_3$ (GH06: $E_{\rm ads}$ = 6300 K, UMIST2012: $E_{\rm ads}$ = 4000 K). A more general overview of the uncertainties around adsorption energies and a critical review can be found in Cuppen et al. (2017). We compare in the following three sets of adsorption energies: Aikawa et al. (1996; model 1), Garrod & Herbst (2006; model 5) and UMIST2012 (model 6).

Differences in the adsorption energies affect most species masses by less than a factor 2–3. However, a few species change by more than a factor of three, some even by an order of magnitude: CN, HCN, CO_2, NH_2, N_2, N_2H^+, Si, SiH, and HCN ice (Fig. 10). The extent of the various ice reservoirs changes from one set of adsorption energies to the other (see Fig. 12). The most extreme case is NH_3 ice where the ice line moves from 40 au ($E_{\rm ads}$ from Aikawa et al. 1996) to 0.3 au ($E_{\rm ads}$ from Garrod & Herbst 2006). We note that a significant change in the ice line does not have to lead to a significant change of the species mass and thus the two provide complementary information. We discuss in the following the processes behind the changes in the chemistry.

- *CO_2*: the snow line limits the radial extent of the CO_2 ring in the midplane of the disk, where water is not yet completely frozen onto the cold dust grains. The snow line changes from ~1 au to ~0.3 au for the two different values of $E_{\rm ads}$ for water, 4800 K and 5700 K. However, none of this affects the water ice reservoir since that is dominated by the mass in the outer disk.
- *CN, HCN, NH_2, N_2*: the adsorption energy of NH_3 ice determines the radial ice line for this species. For $E_{\rm ads}$ = 880 K (Aikawa), the NH_3 ice reservoir extends from 40 to 200 au and nitrogen does not fully condense into NH_3 ice. For $E_{\rm ads}$ = 5530 K (GH06, UMIST2012), all nitrogen is bound in NH_3 ice between 0.3 and 200 au. With a low adsorption energy, sufficient nitrogen remains in the gas phase between 1 and 10 au to form CN, HCN, NH_2, and N_2. Figure 10 shows that all these species have lower masses in case of the higher adsorption energy (GH06, UMIST2012), while the mass of NH_3 ice increases by a factor three.
- *N_2H^+*: the ice line for several ice species, particularly also CO, shifts upward beyond 20 au, if the UMIST2012 adsorption energies are used instead of the Aikawa et al. (1996) ones. This increases the abundance of N-bearing species in the region which is oxygen poor. Since N_2H^+ resides in a thin layer at the disk surface, this extra reservoir causes an increase in mass by a factor of approximately ten.
- *Si, SiH*: the change in the mass of Si and SiH is related to CO_2. In models with a low adsorption energy for water, the CO_2 ring is extended out to a few au. In this ring, CO_2 reacts with Si to form SiO which subsequently freezes out onto the cold dust grains, driving Si into SiO ice at the expense also of the SiH abundance. In the models with a high adsorption energy, Si remains atomic out to a few au. The SiO that forms is efficiently destroyed by reactions with C^+ into Si^+ which is then subsequently neutralized by charge exchange with Mg and Na.

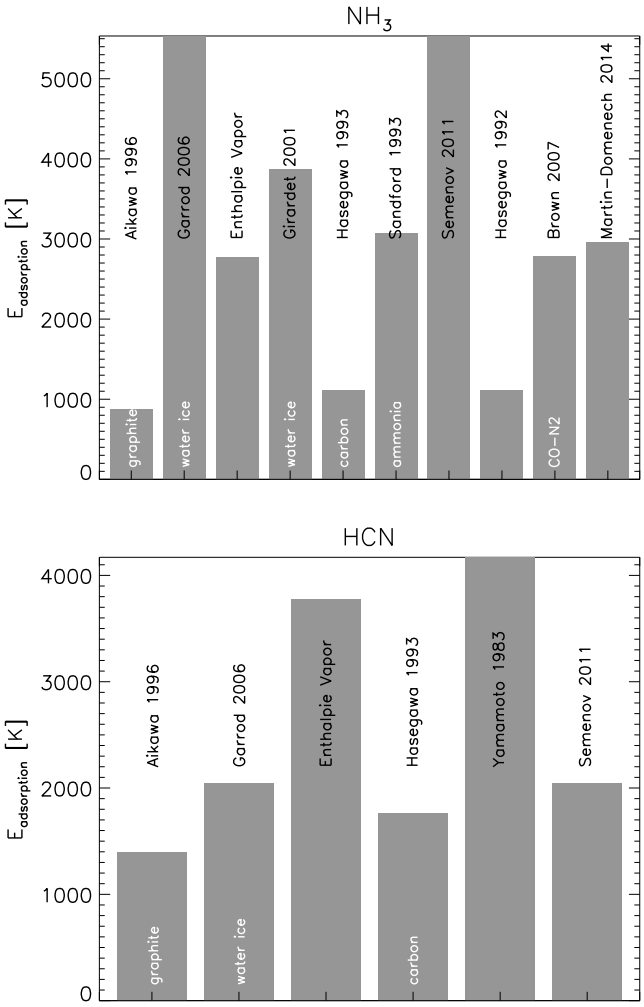

Fig. 9. Comparison between various literature values for the adsorption energy of NH_3 and HCN. White text indicates the surface on which the adsorption energy was measured, so bare carbonaceous grains, ammonia ice, water ice or an ice mixture; black text are the references.

Despite the fact that several gas species masses change drastically, none of the lines studied here is affected by more than a

[2] Details on the various thermal and non-thermal desorption processes can be found in Woitke et al. (2009a).

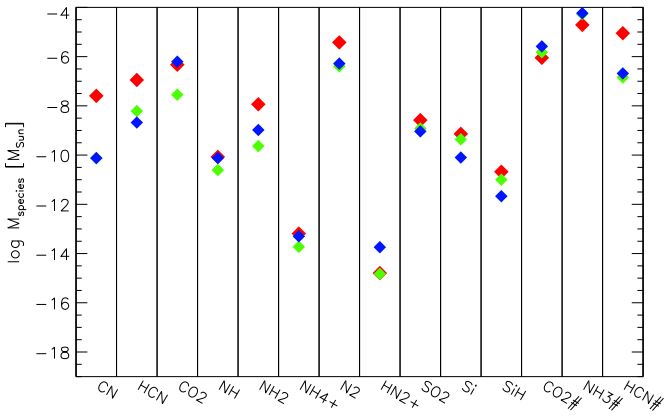

Fig. 10. Differences in species masses between three different sets of adsorption energies: Aikawa et al. (1996; red, model 1), Garrod & Herbst (2006; green, model 5) and McElroy et al. (2013, UMIST2012; blue, model 6). Shown are only species that differ by a factor three or more.

Table 8. Adsorption energies used in the two temperature regimes: bare grains and polar ices.

Ice	E_{ads} [K]			
species	$T > 110$ K	Ref.	$110 \leq T \leq 10$ K	Ref.
CO	960	A96	1150	UMIST2012
H_2O	4800	H09	5700	GH06
CO_2	2000	A96	2990	UMIST2012
CH_4	1360	HH93	1090	UMIST2012
NH_3	880	A96	3874	G01
SO_2	2400	A96	5330	UMIST2012
O_2	960	as CO	1000	UMIST2012
HCN	1400	A96	2050	UMIST2012
N_2	660	scaled CO	1870	G01

Notes. Abbreviations for references can be found in Table A.1.

factor of two except the N_2H^+ line (Figs. B.1 and B.2). Most of the lines are optically thick and/or originate in the disk surface and do not trace the chemistry changes occurring typically closer to the midplane. The only lines changing by a factor of two are the optically thin lines of $C^{18}O$ (1365.42 and 910.31 μm), and the CN line (528.78 μm). The N_2H^+ line at 1072.56 μm increases by more than a factor of ten if the UMIST2012 adsorption energies are used; this is related to the increase in N_2H^+ mass as shown in Fig. 10 due to the change in N_2 absorption energy (GH06: 1000 K, UMIST: 790 K). Apart from the line flux changes, Fig. 11 shows that the N_2H^+ density distributions and therefore also emitting regions in the disk change depending on the set of adsorption energies used.

It is reasonable to assume that the adsorption energy of a specific molecule will depend on the surface property of the grain, that is bare surfaces and/or the polarity of the ice. Hence, we ran an additional model in which we vary the adsorption energy as a function of temperature (model 7). For that we assume two temperature intervals: (1) bare grain surface values for $T > 110$ K; and (2) polar ice values for $110\ \mathrm{K} \leq T \leq 10$ K. Table 8 summarizes the values and regimes for the ices used in the small chemical network. The N_2 adsorption energy is now scaled by a factor 0.7 with respect to the one by Aikawa et al. (1996); such a scaling has already been proposed by Bergin & Langer (1997). Ceccarelli & Dominik (2005) show that such a scaling is required to match H_2D^+ observations and Rab et al. (in prep.) show that it matches typical N_2H^+ line fluxes from disks. Again, the disk density and thermal structure is kept constant.

Figure 13 shows the change in species masses with respect to the Aikawa adsorption energy set for those species that change by a factor three or more: CN, HCN, CO_2, NH, NH_2, NH_4^+, N_2, N_2H^+, O_2^+, SO, CO_2 ice, NH_3 ice and HCN ice. The species masses of the temperature-dependent case sometimes follow the bare grain case and sometimes the water ice surface case. Species with high abundances in the inner disk such as CO_2 stay close to the results from bare grains since this is in fact the adsorption energy that governs their behavior in the temperature-dependent case. Most other species stay close to the results from water ice surfaces since they are dominated by the behavior in the outer disk where grains are covered by water ice. A few species deviate from this, N_2H^+, O_2^+ and SO. In these three cases, the temperature dependent adsorption energies always yield smaller species masses than any of the other two models. This is related to the higher value of N_2 adsorption energy in the temperature range $110 \leq T \leq 10$ K (Girardet & Toubin 2001, on water ice), which allows nitrogen to deplete from the gas phase at smaller radii than in the other two models. This impacts many nitrogen bearing species, but also those which form through nitrogen chemistry including for example gas phase water beyond 10 au.

None of the lines in our selection changes by more than a factor two with respect to the bare grain case (Aikawa et al. 1996) except the N_2H^+ line (see Fig. B.3). The latter becomes a factor six weaker in the case of temperature-dependent adsorption energies. The largest changes in the chemical composition are seen in the ice reservoir inside 100 au (Fig. 12); however most lines originate well above the surface ice line.

3.5. Reactions of excited H_2

We discuss the compilation of reaction rates for excited H_2 (denoted throughout the rest of the paper as H_2^*) in Appendix A.4, where we assume a representative excitation state of $v = 1$ ($E = 5980$ K). It is assumed that 90% of the UV absorption leads to excited H_2, 10% to dissociation (Tielens & Hollenbach 1985).

We find from our standard model that the molecular ions CH^+ and HCO^+ are the most affected species. In both cases, the key reaction is

$$H_2(v = 1) + C^+ \rightarrow CH^+ + H. \quad (4)$$

We use here the updated rate from Eq. (A.5) as explained in the Appendix. The mass of CH^+ increases by a factor ~10 due to the presence of excited H_2 chemistry. All other species masses change by less than 10%. The change in CH^+ abundance transmits through various channels into CH_2^+, CH_3^+ and all those molecular ions have a pathway to form HCO^+

$$CH^+ + H_2O \rightarrow HCO^+ + H_2, \quad (5)$$
$$CH_2^+ + O \rightarrow HCO^+ + H, \quad (6)$$
$$CH_3^+ + O \rightarrow HCO^+ + H_2. \quad (7)$$

However, there are also many alternative pathways forming and destroying HCO^+ that do not involve H_2^*. Hence, the species changes much less than CH^+.

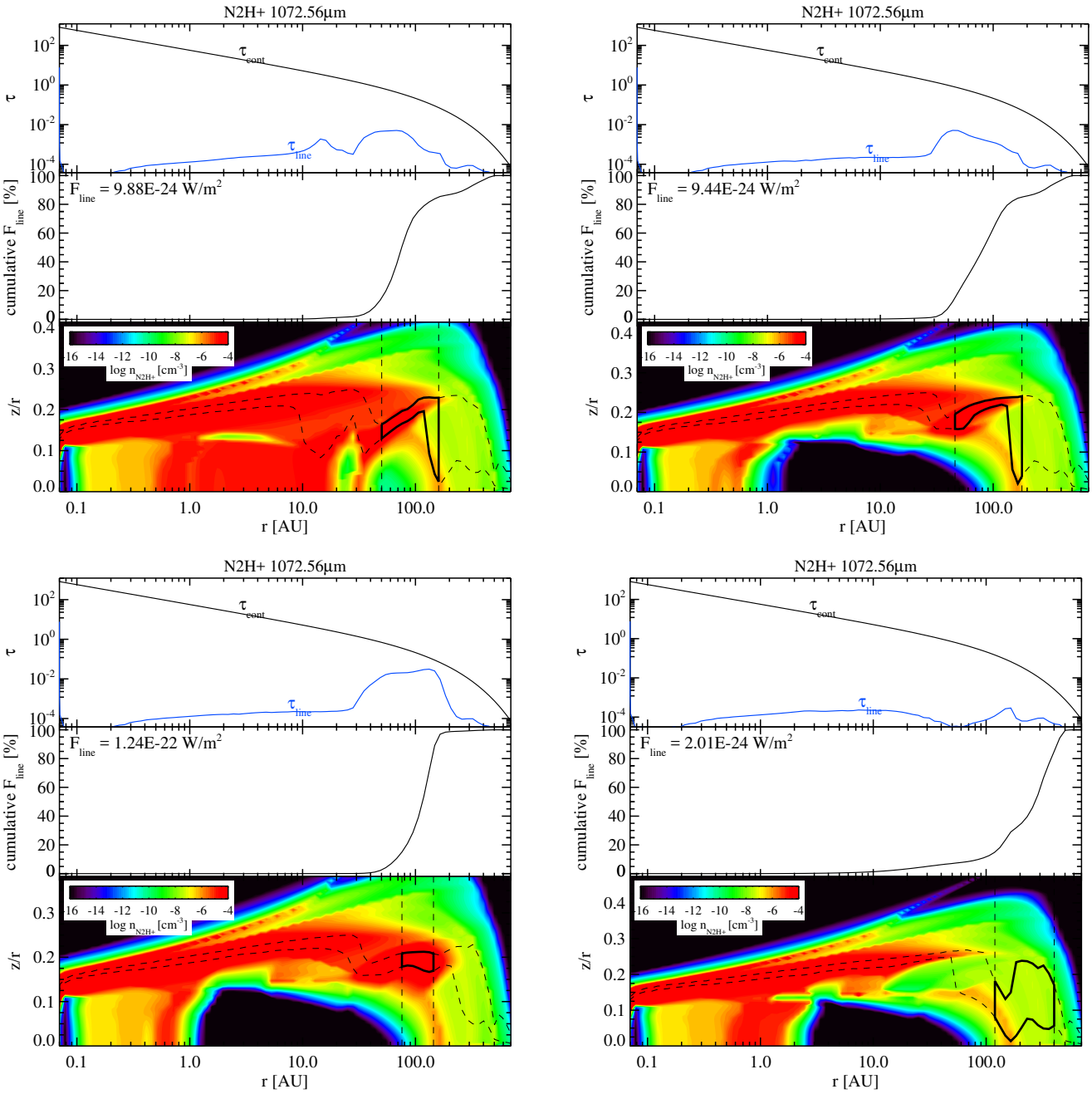

Fig. 11. N_2H^+ $J = 3-2$ line (1072.56 μm) from vertical escape for the four models *from top left to bottom right*: the standard disk model using the set of adsorption energies from Aikawa et al. (1996; model 1), Garrod & Herbst (2006; model 5), UMIST2012 (model 6), T-dependent adsorption rates (model 7). The three panels show the optical depth in the line and the continuum, the cumulative line flux as a function of radius and the box (thick black line) in which 50% of the line flux originates (15–75% radially and vertically – dashed black lines) on the color background of the N_2H^+ density distribution.

3.6. Large versus small networks

With the advent of ALMA, more complex molecular species and especially molecular ions will be detected in many more disks. Hence, we compare the use of small versus large networks. Again, we keep the disk density and thermal structure fixed and compare model 6 (100 species, 1288 reactions) to model 8 (235 species, 3167 reactions) using the UMIST2012 chemical database and adsorption energies.

Figures 14 and 15 show differences at the outermost radii due to the presence of more complex ices. Those affect also the outer water, HCO^+ and HCN reservoirs. Most of these changes come from new branches of chemistry allowed in the larger network such as C-chain chemistry (C_nH_m), more links between the nitrogen, oxygen and carbon chemistry networks through C−N and N−O bearing species, and sulfur chemistry. In addition, the presence of additional ices and PAHs (with their ice counterpart) changes the electron abundance in the disk. Hydrocarbons change in some cases by several orders of magnitude in species mass (e.g., CH_3, CH_4 and CH_5^+ in Fig. 16). In addition, many hydronitrogens (azanes) change in mass between a factor three to ten (e.g., NH_2, NH_3^+, NH_4^+, N_2H^+). Differences in molecular species mass beyond a factor of ten are also seen for H_3^+ (∼1.2 dex), NO^+ (∼1.3 dex), H_3O^+ (∼1 dex), SiH (∼1.8 dex), and $SiOH^+$ (∼1 dex). Many metals and metal ions also change their species masses by more than a factor three. For the ices

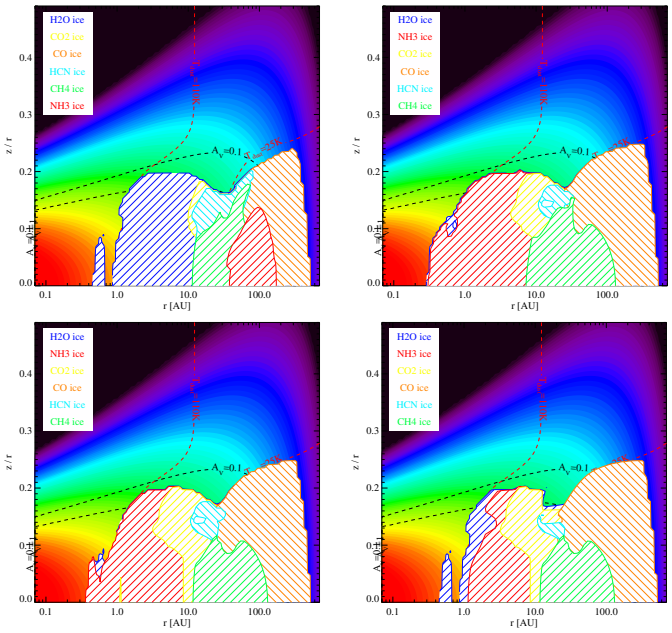

Fig. 12. Distribution of ice reservoirs plotted on top of each other in order from top to bottom of legend. Note that some ices may be partially hidden behind others. The order but not the color scheme is changed for the *upper left panel* to make the ammonia ice visible. *From top left to bottom right*: the standard disk model using the set of adsorption energies from Aikawa et al. (1996; model 1), Garrod & Herbst (2006; model 5), UMIST2012 (model 6), T-dependent adsorption rates (model 7). The color scale in the background shows the total hydrogen number density in the disk model and the black dashed lines the $A_V = 0.1$ and 1 contours (minimum of radial and vertical A_V).

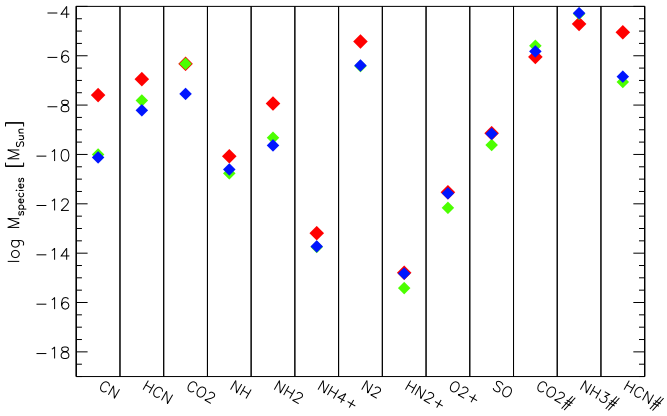

Fig. 13. Differences in species masses between E_{ads} of Aikawa et al. (1996, red, model 1 – bare grains), temperature-dependent adsorption energies (green, model 7) and E_{ads} of Garrod & Herbst (2006, blue, model 5 – water ice).

in common, the largest changes are seen in CH_4 ice (~1.8 dex), SO_2 ice (~1.4 dex) and HCN ice (~1.5 dex).

Figure 17 reveals that the majority of lines investigated here do not change when we expand the chemical network to include more complex chemistry. Some lines change within a factor three, something easily buried in uncertainties within other disk input parameters; examples are the fine-structure lines of neutral carbon at 609 and 370 μm. The sub-mm lines of HCN decrease in the larger network by more than a factor three.

HCO^+ and N_2H^+ lines increase by more than an order of magnitude when the larger network is considered. For HCO^+,

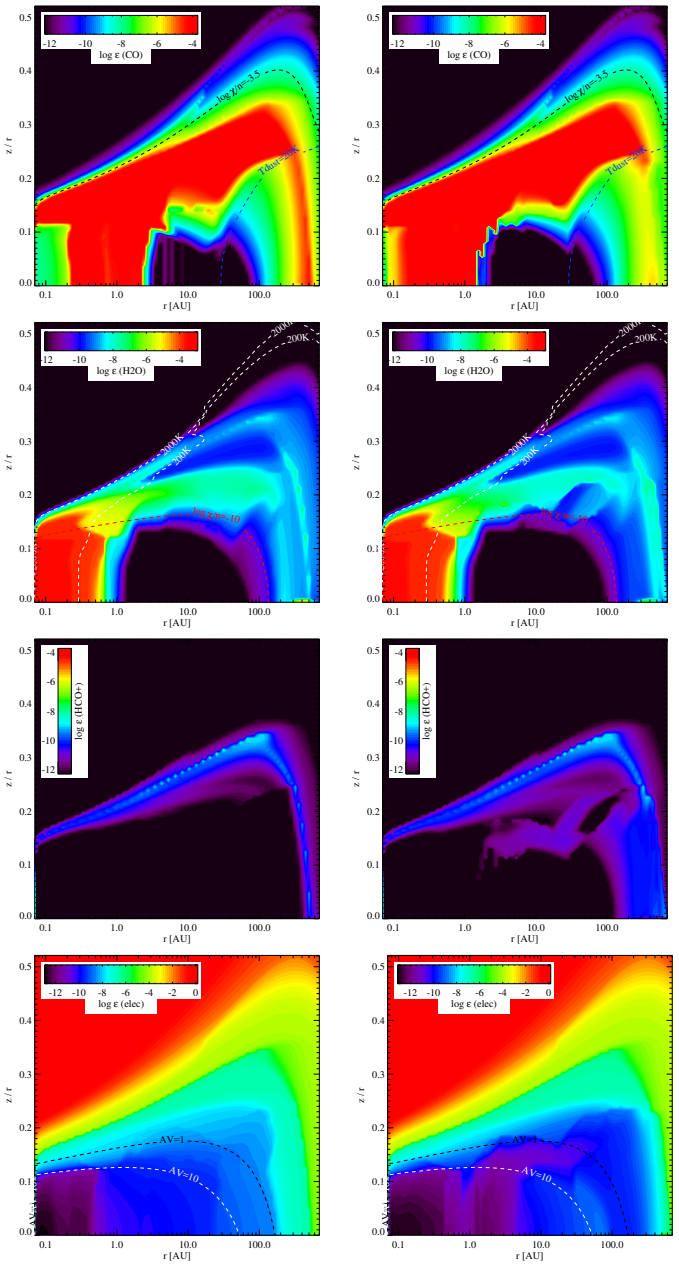

Fig. 14. Distribution of key species abundances using the small (*left*) and large (*right*) chemical network: CO, H_2O, HCO^+, and electrons. Contours are the same as Fig. 1.

this is due to a decrease in electron abundance in the regions where this molecule can form (see Fig. 17), especially in the outer disk beyond 100 au. The change in electron abundance (see Fig. 14) is related to the freeze out of all neutral molecules and atoms (e.g., also sulfur and iron) included in the large network; the small network comprises only freeze-out of the molecules CO, H_2O, CO_2, CH_4, NH_3, SiO, SO_2, O_2, HCN and N_2. More chemical details behind these changes are explained in Rab et al. (2017) with the caveat that they only use the large chemical network.

4. Discussion

Most of the results outlined above are not specific to the choice of thermo-chemical disk code. We fixed the disk structure and exploited purely changes related to the choice of chemical

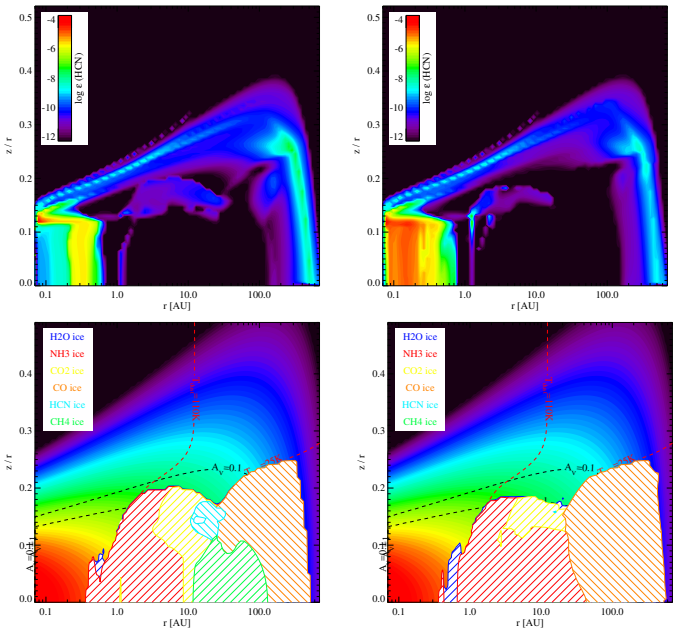

Fig. 15. Distribution of key species abundances using the small (*left*) and large (*right*) chemical network: HCN and ice reservoirs. Contours and legend are the same as Fig. 12.

database, set of adsorption energies and size of the network. Similar changes would show in any chemical code if it is applied to the large range of physical and irradiation conditions in disks. It has to be kept in mind that the chemical databases used in astrochemistry were originally developed for low density cold environments such as molecular clouds. Networks extending to higher temperatures more appropriate for inner disk regions have been developed (e.g., Agúndez et al. 2008; Harada et al. 2010), but are not routinely included in disk chemical models. With this work, we thus push the existing widely-used databases into regimes they have originally not been tested for.

Contrary to McElroy et al. (2013) we find large differences when comparing different chemical databases. We calculate the chemistry in environments of higher densities ($\gtrsim 10^8$ cm^{-3}) and temperatures (10−5000 K), while McElroy et al. (2013) used a dark cloud environment with $n(H_2) = 10^4$ cm^{-3}, $T = 10$ K, $A_V = 10$ mag. Hence, we find differences both in the spatial distribution of species and also in the resulting line fluxes. The differences for OH and water between UMIST and OSU/KIDA can likely be attributed to collider reactions. In addition, many lines originating from the inner disk show changes larger than a factor two. This indicates differences in the warm chemistry between the networks; abundances of many even simple molecules change in the inner disk where gas temperatures are in excess of a 300 K. These differences would not show up under the low density and low temperature conditions of a dark cloud.

The tests with different sets of adsorption energies shows that most atomic and molecular lines do not depend on these values. Many of these lines are optically thick and hence originate largely in the surface layers well above the ice reservoirs. However, the C^{18}O lines are optically thin and therefore directly linked to the size and height of the CO ice reservoir. The fluxes and emission maps of C^{18}O will depend on the details of how ices are treated within the chemical network. Another optically thin line is CN 528.78 μm. If adsorption energies from bare grains are used, the nitrogen reservoir changes significantly and the CN line has an additional contribution from regions inside 100 au. Yet another optically thin line is N_2H^+. The emitting region and also column densities of this species depend crucially on the choice of N_2 adsorption energy and especially also the relative difference between CO and N_2 adsorption energies.

It has been shown by Agúndez et al. (2010) that reactions with excited H_2 play an important role in the formation of CH^+ in diffuse clouds and in Photon Dominated Regions (PDRs). The authors also point out the possible relevance to circumstellar disks. Our tests show now that state-to-state chemical reactions in disks affect indeed mostly CH^+; the effect on other molecular ions is minor. Hence for the interpretation of line fluxes and rotational diagrams of CH^+ such as presented in Thi et al. (2011a) and Fedele et al. (2013), it is important to take reactions with excited H_2 into account.

Semenov et al. (2004) found that especially the intermediate layers of disks where ion-molecule chemistry is active require larger chemical networks in excess of 100 species. However, they focussed largely on the ionization degree to inform MHD disk models and their model assumes that gas and dust temperatures are equal. The latter assumption leads to colder disk surface layers compared to our model. Many neutral-neutral reactions with barriers become only important for gas temperatures above 300 K. Our comparison between the small (100 species, 1288 reactions) and large (235 species, 3167 reactions) network shows the importance of additional freeze-out due to the presence of more ice species. As Semenov et al. (2004), we note the importance of carbon chain chemistry. The new chemical pathways opened by connecting C−N, N−O and sulfur chemistry affect the abundance distribution of species even in the outer disk. The emission lines affected by this are mostly HCN, N_2H^+ and HCO^+, while the CO and CN lines stay within a factor of approximately two. Hence, for the interpretation of submm maps and emission lines of HCN, N_2H^+ and HCO^+, we recommend the use of larger chemical networks and a careful treatment of the ionization (metal abundances, freeze-out, charge exchange and grain charging).

The effects outlined above are all related to differences in the chemical input data. It is widely known that many of the rates we use bear large uncertainties and some reaction pathways may be even debated. In addition, we did not even include surface chemistry here, a new layer of complexity with even more unknown parameters. It becomes clear that interpreting absolute column densities of fluxes from molecular lines will be affected by the specific choice of database and/or size of the network used. This poses especially a problem when comparing works from different groups using different chemical input data. It also puts a limit to the quantitative interpretation of individual line observations. A more robust approach could be a differential investigation of the impact of specific disk parameters on key observables, such as for example the flaring angle, the gas mass, the amount of irradiation. Even though the absolute column densities of specific species may not be known to better than a factor few, the relative changes should be trustable.

5. Conclusions

From the detailed investigation of various chemical databases, different sets of adsorption energies and sizes of chemical networks, we conclude the following key points.

Many atomic and molecular lines are very robust against changes in the chemical rates and in the size of the network. Caution, however, is required for

– HCN, N_2H^+ and HCO^+ lines (size of the network),

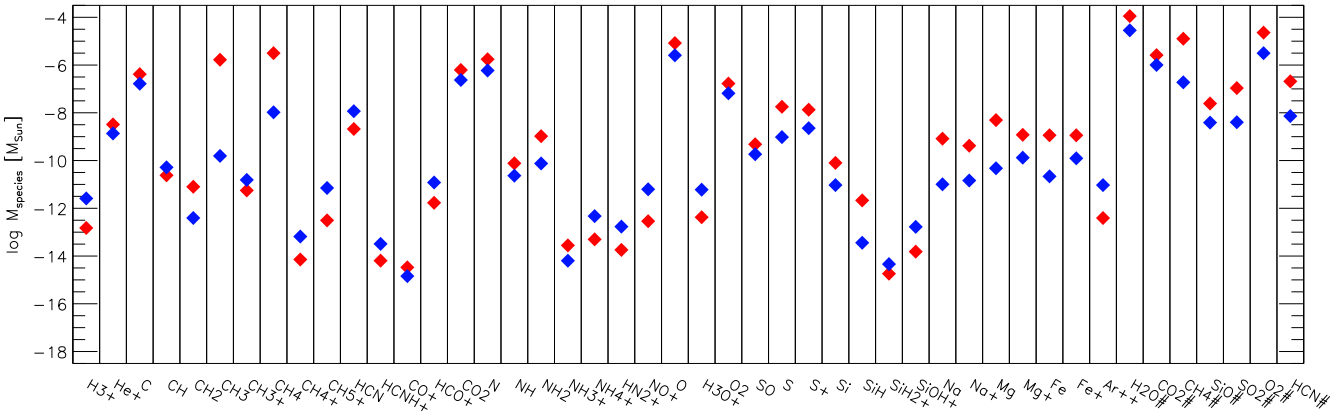

Fig. 16. Differences in species masses using the UMIST2012 database and its adsorption energies for the small (red, model 6) and large chemical network (blue, model 8).

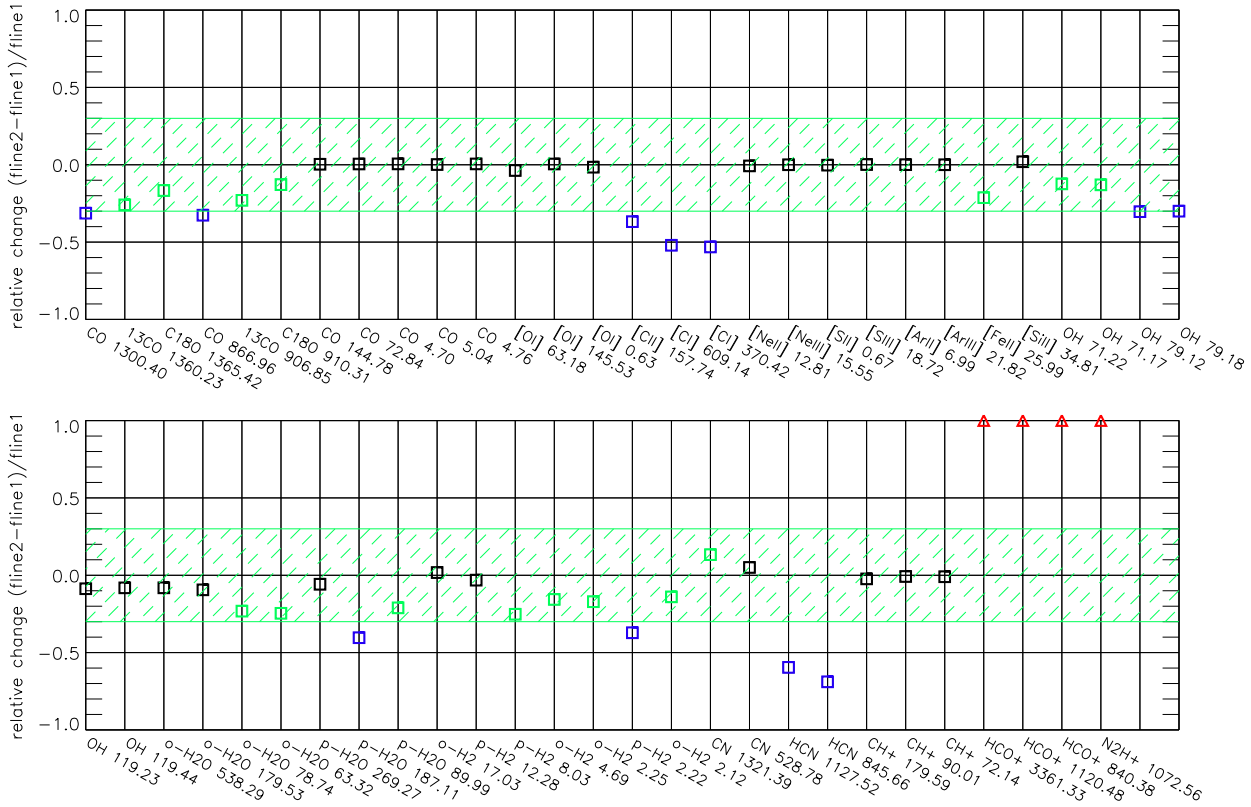

Fig. 17. Comparison of line fluxes using the UMIST2012 database and its adsorption energies for the small (fline1, model 6) and large chemical network (fline2, model 8). Black and green squares denote differences of less than 25% and less than a factor two respectively, blue squares and red triangles denote differences larger than a factor three and ten respectively.

- high excitation CO, CN, CH^+, H_2O, OH lines (database dependency),
- CH^+ lines (reactions of excited H_2),
- HCO^+ lines (UMIST2006 to UMIST2012 update in rates).

Collider reactions play a major role even in the upper layers of disks. Hence, it would be good to revisit those in experiments. Special attention should be given to checking their low temperature extrapolations.

There is not a single consistent set of adsorption energies to be used for disks. Instead, we recommend a self-consistent approach, where the adsorption energy depends on the nature of the already existing ice, for example polar or non-polar. This is of minor importance for most of the observed gas lines. However, it will affect the spatial position of ice lines in the disk and thus the emitting region of the rarer CO isotopologues and molecular ions such as HCO^+ and N_2H^+.

For CH^+ state-to-state reactions become important in the upper layers of disks. Only very few reactions of excited molecular hydrogen have so far been investigated in detail. The here proposed simplified scheme of using the H_2 $v = 1$ state and scaling the known reaction rates for H_2 $v = 0$ can only be a first step.

As demonstrated here, the absolute line fluxes can be very sensitive to the specific choice of rate network. However, this will not affect studies where the sensitivity of lines is tested against specific disk parameters using the same chemical network and database. However, discrepancies in disk models for

specific objects from groups using different chemical networks should be taken with caution.

More recent discussions among the disk modelers and the chemical database groups start to diminish some of the discrepancies noted in this work. Hence, we expect that new database releases will bring the results in even closer agreement.

Acknowledgements. We would like to thank K. Oeberg, E. Bergin, T. Millar and E. van Dishoeck for insightful discussions during the development of this work. We also thank the anonymous referee for a careful reading of the manuscript and suggestions that improved the clarity of the figures and text. I.K., W.F.T., C.R., and P.W. acknowledge funding from the EU FP7-2011 under Grant Agreement No. 284405. C.R. also acknowledges funding by the Austrian Science Fund (FWF), project number P24790.

References

Ádámkovics, M., Glassgold, A. E., & Meijerink, R. 2011, ApJ, 736, 143
Agúndez, M., Cernicharo, J., & Goicoechea, J. R. 2008, A&A, 483, 831
Agúndez, M., Goicoechea, J. R., Cernicharo, J., Faure, A., & Roueff, E. 2010, ApJ, 713, 662
Aikawa, Y., & Herbst, E. 2001, A&A, 371, 1107
Aikawa, Y., Miyama, S. M., Nakano, T., & Umebayashi, T. 1996, ApJ, 467, 684
Anicich, V. G. 1993, J. Phys. Chem. Ref. Data, 22, 1469
Antonellini, S. 2016, Ph.D. Thesis, Kapteyn Astronomical Institute, University of Groningen, Landleven 12, 9700 AV Groningen, The Netherlands
Antonellini, S., Kamp, I., Riviere-Marichalar, P., et al. 2015, A&A, 582, A105
Aresu, G., Kamp, I., Meijerink, R., et al. 2011, A&A, 526, A163
Aresu, G., Meijerink, R., Kamp, I., et al. 2012, A&A, 547, A69
Avramenko, L. I., & Krasnenkov, V. M. 1966, Bull. Acad. Sci. USSR Div. Chem. Sci. (Engl. Transl.), 15, 394
Badnell, N. R. 2006, ApJS, 167, 334
Badnell, N. R., O'Mullane, M. G., Summers, H. P., et al. 2003, A&A, 406, 1151
Baulch, D. L., Cobos, C. J., Cox, R. A., et al. 1992, J. Phys. Chem. Ref. Data, 21, 411
Bergin, E. A., & Langer, W. D. 1997, ApJ, 486, 316
Bergin, E. A., Langer, W. D., & Goldsmith, P. F. 1995, ApJ, 441, 222
Bethell, T. J., & Bergin, E. A. 2011, ApJ, 739, 78
Björk, J., Stafström, S., & Hanke, F. 2011, J. Am. Chem. Soc., 133, 14884
Bouwman, J., Cuppen, H. M., Steglich, M., Allamandola, L. J., & Linnartz, H. 2011a, A&A, 529, A46
Bouwman, J., Mattioda, A. L., Linnartz, H., & Allamandola, L. J. 2011b, A&A, 525, A93
Ceccarelli, C., & Dominik, C. 2005, A&A, 440, 583
Ceccarelli, C., Dominik, C., Caux, E., Lefloch, B., & Caselli, P. 2005, ApJ, 631, L81
Cernicharo, J., Ceccarelli, C., Ménard, F., Pinte, C., & Fuente, A. 2009, ApJ, 703, L123
Collings, M. P., Anderson, M. A., Chen, R., et al. 2004, MNRAS, 354, 1133
Cuppen, H. M., Walsh, C., Lamberts, T., et al. 2017, Space Sci. Rev.
De Becker, M. 2013, Bull. Soc. Roy. Sci. Liège, 82, 33
Dere, K. P., Landi, E., Mason, H. E., Monsignori Fossi, B. C., & Young, P. R. 1997, A&AS, 125, 149
Domine, F., Cincinelli, A., Bonnaud, E., Martellini, T., & Picaud, S. 2007, Environmental Science Technology, 41, 6033
Dutrey, A., Henning, T., Guilloteau, S., et al. 2007, A&A, 464, 615
Eiteneer, B., & Frenklach, M. 2003, Int. J. Chem. Kinet., 35, 391
Fedele, D., Bruderer, S., van Dishoeck, E. F., et al. 2013, A&A, 559, A77
Fontijn, A., Shamsuddin, S. M., Crammond, D., Marshall, P., & Anderson, W. R. 2006, Combust. Flame, 145, 543
Fu, J., & Suuberg, E. M. 2011, J. Chem. Thermodyn., 43, 1660
Garrod, R. T., & Herbst, E. 2006, A&A, 457, 927
Girardet, C., & Toubin, C. 2001, Surface Sci. Rep., 44, 159
Glassgold, A. E., Meijerink, R., & Najita, J. R. 2009, ApJ, 701, 142
Goldfarb, J. L., & Suuberg, E. M. 2008, J. Chem. Engng. Data, 53, 670
Harada, N., Herbst, E., & Wakelam, V. 2010, ApJ, 721, 1570
Hasegawa, T. I., & Herbst, E. 1993, MNRAS, 261, 83
Heays, A. N., Bosman, A. D., & van Dishoeck, E. F. 2017, A&A, 602, A105
Hierl, P. M., Morris, R. A., & Viggiano, A. A. 1997, J. Chem. Phys., 106, 10145
Hily-Blant, P., Bonal, L., Faure, A., & Quirico, E. 2013, Icarus, 223, 582
Hollenbach, D., & McKee, C. F. 1989, ApJ, 342, 306
Hollenbach, D. J., Takahashi, T., & Tielens, A. G. G. M. 1991, ApJ, 377, 192
Hollenbach, D., Kaufman, M. J., Bergin, E. A., & Melnick, G. J. 2009, ApJ, 690, 1497
Jodkowski, J. T., Rayez, M.-T., & Rayez, J.-C. 1999, J. Phys. Chem. A, 103, 3750
Jones, M. E., Barlow, S. E., Ellison, G. B., & Ferguson, E. E. 1986, Chem. Phys. Lett., 130, 218
Kamp, I., Tilling, I., Woitke, P., Thi, W., & Hogerheijde, M. 2010, A&A, 510, A18
Kamp, I., Thi, W.-F., Meeus, G., et al. 2013, A&A, 559, A24
Koshi, M., Yoshimura, M., Fukuda, K., & Matsui, H. 1990, J. Chem. Phys., 93, 8703
Kruse, T., & Roth, P. 1997, J. Phys. Chem. A, 101, 2138
Kumar, S., Parks, D., & Kamrin, K. 2016, ACS Nano, 10, 6552
Landini, M., & Fossi, B. C. M. 1991, A&AS, 91, 183
Lee, H.-H., Roueff, E., Pineau des Forets, G., et al. 1998, A&A, 334, 1047
Lennon, M. A., Bell, K. L., Gilbody, H. B., et al. 1988, J. Phys. Chem. Ref. Data, 17, 1285
McElroy, D., Walsh, C., Markwick, A. J., et al. 2013, A&A, 550, A36
Mebel, A., Moskaleva, L. V., & Lin, M. C. 1999, J. Mol. Struct. Theochem., 461, 223
Meijerink, R., Aresu, G., Kamp, I., et al. 2012, A&A, 547, A68
Mészár, Z. E., Hantal, G., Picaud, S., & Jedlovszky, P. 2013, J. Phys. Chem. C, 117, 6719
Min, M., Bouwman, J., Dominik, C., et al. 2016a, A&A, 593, A11
Min, M., Rab, C., Woitke, P., Dominik, C., & Ménard, F. 2016b, A&A, 585, A13
Nomura, H., & Millar, T. J. 2005, A&A, 438, 923
Öberg, K. I., Qi, C., Fogel, J. K. J., et al. 2010, ApJ, 720, 480
Oja, V., & Suuberg, E. M. 1998, J. Chem. Engng. Data, 43, 486
Panić, O., & Hogerheijde, M. R. 2009, A&A, 508, 707
Pierson, H. O. 1993, Handbook of carbon, graphite, diamond and fullerenes (New Jersey: Noyes)
Prasad, S. S., & Huntress, Jr., W. T. 1980, ApJS, 43, 1
Qi, C., Kessler, J. E., Koerner, D. W., Sargent, A. I., & Blake, G. A. 2003, ApJ, 597, 986
Qi, C., Öberg, K. I., & Wilner, D. J. 2013a, ApJ, 765, 34
Qi, C., Öberg, K. I., Wilner, D. J., et al. 2013b, Science, 341, 630
Rab, C., Güdel, M., Padovani, M., et al. 2017, A&A, 603, A96
Sandford, S. A., & Allamandola, L. J. 1993, ApJ, 417, 815
Schöier, F. L., van der Tak, F. F. S., van Dishoeck, E. F., & Black, J. H. 2005, A&A, 432, 369
Semenov, D., Wiebe, D., & Henning, T. 2004, A&A, 417, 93
Sternberg, A., & Dalgarno, A. 1995, ApJS, 99, 565
Thi, W.-F., van Zadelhoff, G.-J., & van Dishoeck, E. F. 2004, A&A, 425, 955
Thi, W.-F., Ménard, F., Meeus, G., et al. 2011a, A&A, 530, L2
Thi, W.-F., Woitke, P., & Kamp, I. 2011b, MNRAS, 412, 711
Thi, W. F., Kamp, I., Woitke, P., et al. 2013, A&A, 551, A49
Thrower, J. D., Collings, M. P., Rutten, F. J. M., & McCoustra, M. R. S. 2009a, MNRAS, 394, 1510
Thrower, J. D., Collings, M. P., Rutten, F. J. M., & McCoustra, M. R. S. 2009b, J. Chem. Phys., 131, 244711
Thrower, J. D., Friis, E. E., Skov, A. L., et al. 2013, J. Phys. Chem. C, 117, 13520
Tielens, A. G. G. M., & Hollenbach, D. 1985, ApJ, 291, 722
Tielens, A. G. G. M., Allamandola, L. J., Barker, J. R., & Cohen, M. 1987, in NATO Advanced Science Institutes (ASI) Series C 191, eds. A. Leger, L. D'Hendecourt, & N. Boccara, 273
Tsang, W. 1987, J. Phys. Chem. Ref. Data, 16
Tsang, W., & Hampson, R. F. 1986, J. Phys. Chem. Ref. Data, 15
van Dishoeck, E. F. 1990, in The Evolution of the Interstellar Medium, ed. L. Blitz, ASP Conf. Ser., 12, 207
van Dishoeck, E. F., Jonkheid, B., & van Hemert, M. C. 2006, Faraday Discussions, 133, 231
Vasyunin, A. I., Sobolev, A. M., Wiebe, D. S., & Semenov, D. A. 2004, Astron. Lett., 30, 566
Vasyunin, A. I., Semenov, D., Henning, T., et al. 2008, ApJ, 672, 629
Verner, D. A., & Yakovlev, D. G. 1995, A&AS, 109, 125
Visser, R., Geers, V. C., Dullemond, C. P., et al. 2007, A&A, 466, 229
Wakelam, V., Herbst, E., Loison, J.-C., et al. 2012, ApJS, 199, 21
Woitke, P., Kamp, I., & Thi, W.-F. 2009a, A&A, 501, 383
Woitke, P., Thi, W.-F., Kamp, I., & Hogerheijde, M. R. 2009b, A&A, 501, L5
Woitke, P., Riaz, B., Duchêne, G., et al. 2011, A&A, 534, A44
Woitke, P., Min, M., Pinte, C., et al. 2016, A&A, 586, A103
Woodall, J., Agúndez, M., Markwick-Kemper, A. J., & Millar, T. J. 2007, A&A, 466, 1197
Zanchet, A., Agúndez, M., Herrero, V. J., Aguado, A., & Roncero, O. 2013a, AJ, 146, 125
Zanchet, A., Godard, B., Bulut, N., et al. 2013b, ApJ, 766, 80
Zatsarinny, O., Gorczyca, T. W., Korista, K. T., Badnell, N. R., & Savin, D. W. 2003, A&A, 412, 587
Zhu, W., Zhang, J. Z. H., Zhang, Y. C., Zhang, Y. B., & Zhan, L. X. 1998, J. Chem. Phys., 108, 3509

Appendix A: Chemical reaction rates

Next to the standard rates from chemical databases such as UMIST, OSU or KIDA, we use the additional set of reaction rates described below. Some of them are added to the standard set of rates, some overwrite rates from the databases if this option is invoked. This is indicated in the respective subsections. Abbreviations for the references are listed in Table A.1.

A.1. Chemistry different from UMIST

A key reaction is the H_2 formation which is hardcoded in ProDiMo. The reaction rate and implementation is described in Woitke et al. (2009a).

A.2. Chemistry added to UMIST

Reactions which we include in addition to UMIST are given in Table A.2. Most of them describe the photodissociation of molecular ions; these latter rates are taken from Heays et al. (2017). We use the formalism of Woitke et al. (2009a) to implement adsorption of gas phase species onto grains and thermal and non-thermal desorption.

A.3. Photochemistry

We calculate the photo rates from using the local radiation field from the 2D continuum radiative transfer (Kamp et al. 2010) and the photoionization and – dissociation cross sections from the Leiden database (van Dishoeck et al. 2006; Heays et al. 2017). These rates replace the standard UMIST photo rates even if the UMIST database is chosen.

A.4. Chemistry of excited H_2

Reactions of excited H_2 (H2EXC, H_2^*) are neither included in UMIST2006 nor in UMIST2012. They can be important in disks, especially at the surface and thus have been included in Reactions.in. The basic assumption is that the vibrational energy of the excited H_2 can be entirely used to overcome a potential reaction barrier (Tielens & Hollenbach 1985). While this might be a reasonable assumption for low barriers, it may overestimate the rates for reactions with a high barrier. In any case all those rates should be treated as guesses at most. In the absence of any better rates, the reaction rate of a species with H_2 is simply modified by subtracting the energy corresponding to the first vibrational excited level $v = 1$, 5980 K.

The collisional de-excitation rate (in units of cm^3 s^{-1}) of the pseudo excited state (effective quantum number $v = 6$) H_2^* by collisions with H and H_2 is taken from Tielens & Hollenbach (1985) as one-sixth of the collisional de-excitation rate from $v = 1$, $\gamma_{10}^{\rm H,H_2}$

$$R_{ul}^{\rm H} = 2.887\times10^{-12}\left(\frac{T}{300}\right)^{0.5}\exp\left(-1000/T\right), \quad (A.1)$$

$$R_{ul}^{\rm H_2} = 4.042\times10^{-12}\left(\frac{T}{300}\right)^{0.5}\exp\left(-18\,100/(T+1200)\right), \quad (A.2)$$

We note that Tielens & Hollenbach (1985) provide in their Table 9 a de-excitation rate for collisions with atomic hydrogen that is a factor 0.67 smaller than this. The collisional excitation rates (in units of cm^3 s^{-1}) are the inverse of these de-excitation rates (Woitke et al. 2009a) using the energy of the pseudo-level for vibrationally excited H_2, $E_v = 2.6$ eV,

$$R_{lu}^{\rm H} = R_{ul}^{\rm H}\exp\left(-E_v/kT_{\rm gas}\right), \quad (A.3)$$

$$R_{lu}^{\rm H_2} = R_{ul}^{\rm H_2}\exp\left(-E_v/kT_{\rm gas}\right), \quad (A.4)$$

Other rates are taken explicitly from their Table 9.

Agúndez et al. (2010) use for the reaction $H_2^* + C^+ \rightarrow CH^+ + H$ a constant Langevin rate coefficient of 1.6×10^{-9} cm^3 s^{-1}. Figure 10 of Hierl et al. (1997) suggest a possible weak temperature dependence. Zanchet et al. (2013b) performed quantum calculations to derive state-to-state reaction rates for the system C^+ and H_2. In the following, we neglect the formation excitation of CH^+ and use the parametrized rate from Zanchet et al. (2013a) for $H_2(v = 1)$ (Table 3). To bring it into the usual form, we present here a simple Arrhenius fit

$$R = 3.87\times10^{-10}\left(\frac{T}{300}\right)^{-0.136}\exp\left(-4.33/T\right)\ \text{cm}^3\ \text{s}^{-1}. \quad (A.5)$$

The theoretical calculations are a factor of four lower than the laboratory work from Hierl et al. (1997; Fig. A.1). The newer rate is only used in Sect. 3.5 discussing the effect of excited H_2 on the chemistry.

In addition to those reactions, we add

$$H_2^* + CN \rightarrow HCN + H, \quad (A.6)$$

$$H_2^* + He^+ \rightarrow H^+ + H + He, \quad (A.7)$$

taken from Zhu et al. (1998) and Jones et al. (1986), respectively. In the latter case, $R = 0.18{-}1.8\times10^{-9}$ cm^3/s and we approximate that with 0.5×10^{-9} cm^3/s.

$$H_2^* + C_2 \rightarrow C_2H + H, \quad (A.8)$$

$$H_2^* + C_2H \rightarrow C_2H_2 + H, \quad (A.9)$$

Table A.1. List of reference abbreviations.

Abbreviation	Reference
A93	Anicich (1993)
A96	Aikawa et al. (1996)
AG-estimate	Al Glassgold (priv. comm.)
B06	Badnell (2006)
BC92	Baulch et al. (1992)
EF03	Eiteneer & Frenklach (2003)
FS06	Fontijn et al. (2006)
G01	Girardet & Toubin (2001)
H17	Heays et al. (2017)
HH93	Hasegawa & Herbst (1993)
HM89	Hollenbach & McKee (1989)
HM97	Hierl et al. (1997)
HTT91	Hollenbach et al. (1991)
H09	Hollenbach et al. (2009)
JB86	Jones et al. (1986)
JR99	Jodkowski et al. (1999)
KR97	Kruse & Roth (1997)
KY90	Koshi et al. (1990)
L88	Lennon et al. (1988)
LF91	Landini & Fossi (1991)
MM99	Mebel et al. (1999)
TH85	Tielens & Hollenbach (1985)
TH86	Tsang & Hampson (1986)
T87	Tsang (1987)
vD08	van Dishoeck et al. (2006)
VY95	Verner & Yakovlev (1995)
ZZ98	Zhu et al. (1998)

Table A.2. Rate constants for reactions added on top of the UMIST database.

Reaction	A	B	C	Temperature range	Reference
$CH_5^+ + h\nu \rightarrow CH_4^+ + H$	3.00(–11)	0.0	2.0	10.0–41 000.0	H17
$CH_5^+ + h\nu \rightarrow CH_3^+ + H_2$	3.00(–11)	0.0	2.0	10.0–41 000.0	H17
$H_2O + h\nu \rightarrow O + H_2$	8.89(–11)	3.90	4.12	10.0–41 000.0	H17
$H_2O^+ + h\nu \rightarrow O + H_2^+$	5.00(–13)	0.0	2.0	10.0–41 000.0	H17
$H_2O^+ + h\nu \rightarrow O^+ + H_2$	5.00(–13)	0.0	2.0	10.0–41 000.0	H17
$H_3O^+ + h\nu \rightarrow H_2O + H^+$	2.00(–11)	0.0	2.0	10.0–41 000.0	H17
$H_3O^+ + h\nu \rightarrow OH + H_2^+$	1.00(–11)	0.0	2.0	10.0–41 000.0	H17
$H_3O^+ + h\nu \rightarrow H_2O^+ + H$	2.00(–11)	0.0	2.0	10.0–41 000.0	H17
$H_3O^+ + h\nu \rightarrow OH^+ + H_2$	2.00(–11)	0.0	2.0	10.0–41 000.0	H17
$SiOH^+ + h\nu \rightarrow SiO^+ + H$	5.00(–11)	0.0	2.0	10.0–41 000.0	H17
$NH^+ + h\nu \rightarrow N^+ + H$	5.40(–11)	0.0	1.64	10.0–41 000.0	vD08
$C^+ + SiO \rightarrow SiO^+ + C$	5.40(–10)	0.0	0.0	10.0–41 000.0	TH85
$H_2 + H_2 \rightarrow H_2 + H + H$	2.30(–11)	1.25	65 000.0	10.0–41 000.0	TH85
$CO + H \rightarrow HCO$	5.29(–34)	0.0	370.0	10.0–41 000.0	NIST

Notes. The coefficients A, B, and C have their usual meaning (see e.g., McElroy et al. 2013). The notation $x(y)$ denotes $x\,10^y$.

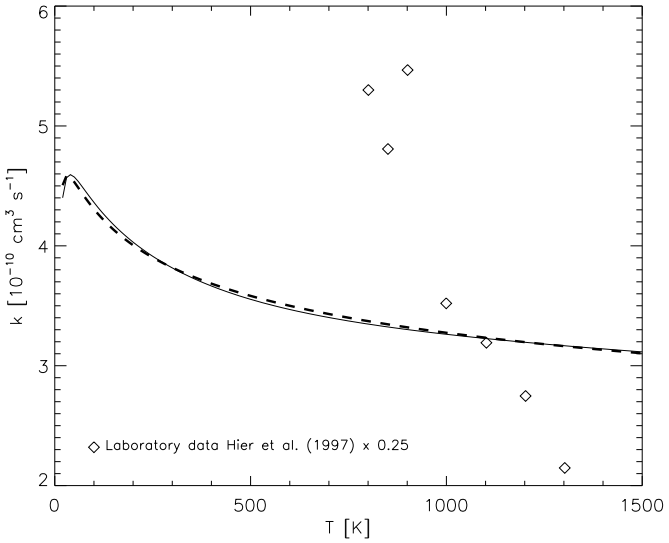

Fig. A.1. Comparison of the theoretically calculated rate A.7 (solid line, Zanchet et al. 2013a), the laboratory data scaled by a factor 0.25 (diamonds, Hierl et al. 1997) and the fit presented here (dashed line).

are taken from NIST (Kruse & Roth 1997; Eiteneer & Frenklach 2003). The activation barriers of 4000 K, 460.6 K (respectively) are set to zero.

$$H_2^* + CH_2 \rightarrow CH_3 + H, \quad (A.10)$$
$$H_2^* + CH_3 \rightarrow CH_4 + H, \quad (A.11)$$

are taken from NIST (Tsang & Hampson 1986; Baulch et al. 1992). The first one has only an upper limit and we use that for the rate and set the activation barrier of 6400 K to 420 K. The activation barrier of 4740 K for the second one is set to zero.

$$H_2^* + CH_3O \rightarrow CH_3OH + H, \quad (A.12)$$
$$H_2^* + CH_2OH \rightarrow CH_3OH + H, \quad (A.13)$$

are taken from NIST (Jodkowski et al. 1999; Tsang 1987). The activation barriers of 2470 K, 6720 K (respectively) are set to zero and 740 K respectively.

$$H_2^* + N \rightarrow NH + H, \quad (A.14)$$
$$H_2^* + NH \rightarrow NH_2 + H, \quad (A.15)$$
$$H_2^* + NH_2 \rightarrow NH_3 + H, \quad (A.16)$$

are taken from NIST (Koshi et al. 1990; Fontijn et al. 2006; Mebel et al. 1999). The activation barriers of 16 600 K, 7760 K, 3610 K (respectively) are set to 12 115 K, 1802 K and zero respectively.

$$H_2^* + C \rightarrow CH + H, \quad (A.17)$$
$$H_2^* + CH \rightarrow CH_2 + H, \quad (A.18)$$

are taken from UMIST2006 and their activation barriers of 11 700 K and 1943 K are set to 5720 K and zero respectively.

$$H_2^* + O \rightarrow OH + H, \quad (A.19)$$
$$H_2^* + OH \rightarrow H_2O + H, \quad (A.20)$$
$$H_2^* + O_2 \rightarrow OH + OH, \quad (A.21)$$

are taken from UMIST2006 and their activation barriers of 3150 K, 1736 K, 21 890 K are set to zero, zero and 15 910 K respectively.

$$H_2^* + H \rightarrow H + H + H, \quad (A.22)$$
$$H_2^* + H_2 \rightarrow H_2 + H + H, \quad (A.23)$$
$$H_2^* + H_2^* \rightarrow H_2 + H + H, \quad (A.24)$$

are taken from UMIST2006 and their activation barriers of 55 000 K, 84 100 K, 84 100 K are set to 49 020 K, 78 120 K, and 72 260 K.

A.5. Collider reactions

Even though UMIST2006 contains collider (three-body reactions, CL), the UMIST2012 rate file does not. There are 32 collider reactions in UMIST2006 (#4552–#4583). After discussion with T. Millar, we decided to append them to the UMIST2012 data file.

A.6. PAH chemistry

PAHs participate in charge exchange reactions with other gas-phase species or the ionized PAHs can recombine with electrons. Therefore PAHs are a key species to the modeling of the gas heating and key to the determination of the ionisation fraction in disks. An example of the role of PAHs is for example that negative PAHs can lock a large fraction of the free electrons, preventing them to recombine with HCO^+ or N_2H^+, two commonly detected species in protoplanetary disks. The PAH reactions are

Table A.3. Measured and computed (Mészár) PAH desorption energies.

Name	Formula	Oja98	Thower09	Domine07	Fu11	Goldfarb08	Meszar13	Thower13
				$E_{\rm des}$ [K]				
benzene	C_6H_6		5431					
naphtalene	$C_{10}H_8$						8448	
acenaphthylene	$C_{12}H_8$					8298 ± 989		
acenaphthene	$C_{12}H_{10}$					9470 ± 269		
fluorene	$C_{13}H_{10}$					1059 ± 229		
anthracene	$C_{14}H_{10}$	12 068				11 848 ± 399		
phenanthrene	$C_{14}H_{10}$	10 860		10 862				
fluoranthene	$C_{16}H_{10}$					11 658 ± 332		
pyrene	$C_{16}H_{10}$	12 442				11 762 ± 392		
2,3-benzofluorene	$C_{17}H_{12}$	14 397						
naphthacene	$C_{18}H_{12}$	15 218				15 006 ± 350		
perylene	$C_{20}H_{12}$	16 003				15 175 ± 98		
benzo[a]phenanthrene	$C_{18}H_{12}$					13 224 ± 430		
benzo[a]pyrene	$C_{20}H_{12}$					13 633 ± 375		
benzo[b]fluoranthene	$C_{20}H_{12}$				14 337			
benzo[k]fluoranthene	$C_{20}H_{12}$				14 663			
benzo[ghi]perylene	$C_{22}H_{12}$				15 448			
indeno[1, 2, 3-cd]pyrene	$C_{22}H_{12}$				15 906			
dibenz[a, h]anthracene	$C_{22}H_{14}$				16 667			
pentacenene	$C_{22}H_{14}$	18 936						
coronene	$C_{24}H_{12}$	16 063						19 727

Notes. Oja98: Oja & Suuberg (1998); Thower09: Thrower et al. (2009b); Domine07: Domine et al. (2007); Fu11: Fu & Suuberg (2011); Goldfarb08: Goldfarb & Suuberg (2008); Meszar13: Mészár et al. (2013); Thrower13: Thrower et al. (2013).

described in details in Thi et al. (in prep.). PAHs can adsorb onto the surfaces of grains and desorb through photons or thermal heating depending on their sizes. PAH freeze-out can modify the heating-cooling balance as well as the ionisation fraction in disks. The ionisation balance is calculated using the local UV radiation field (Woitke et al. 2011). The models described in this paper use circumcoronene ($C_{54}H_{18}$) as the representative PAH. Circumcoronene is a large and compact PAH (pericondensed, superaromatic) and the electron delocalization adds to its stability against photodissociation (Tielens et al. 1987; Visser et al. 2007; De Becker 2013).

A.6.1. PAH freeze-out and desorption

PAHs can adsorb onto grain surfaces coated with water ice or on bare silicate grains. In dense molecular clouds, weak absorption features have been attributed to PAHs frozen in water ice mantles (Bouwman et al. 2011a). Bouwman et al. (2011b) estimated that the PAH_{ice}/H_2O_{ice} ratio can reach as much as 2%. Assuming a water ice abundance of $\sim 10^{-5}$, the PAH# (PAHs adsorbed on dust surfaces) abundance is $\sim 2 \times 10^{-7}$, which suggests that all the PAHs are removed from the gas phase (the total PAH abundance is estimated to be $\sim 3 \times 10^{-7}$). The standard PAH used in the models presented here is circumcoronene although one can choose also larger condensed PAHs such as circumcircumcoronene ($C_{96}H_{24}$), which are even more stable against photodissociation than circumcoronene.

In the absence of measured desorption rates for all individual PAHs, we assume a linear dependance of the desorption energy on the number of carbon and hydrogen atoms of the PAH based on the method of fragment constant. The linear behavior is consistent with the additivity of van der Waals interactions (Björk et al. 2011). Adsorption (desorption) energies $E_{\rm ads}$ measured in the laboratory vary from $E_{\rm ads}/k \simeq 5600$ K for benzene C_6H_6 (Thrower et al. 2009a) up to $E_{\rm ads}/k \simeq 18\,900$ K for pentacenene $C_{22}H_{14}$ (Oja & Suuberg 1998). Table A.3 summarises the adsorption (desorption) energies for several PAHs. It should be noted that the surface on which the PAHs are adsorbed varies in the different studies. We plotted the adsorption energy normalized by the number of carbon atoms $E_{\rm des}/N_{\rm C}$ as a function of $N_{\rm H}/N_{\rm C}$ in Fig. A.3. The adopted law is

$$E_{\rm ads}/k = (482 \times (N_{\rm C} - N_{\rm H)}) + (946 \times N_{\rm H}) \ \ {\rm K}, \tag{A.25}$$

where $N_{\rm C}$ is the number of carbon atoms of the PAH and $N_{\rm H}$ is the number of hydrogen. $E_{\rm CC}/k$ (=482 K) is the fitted desorption energy per graphene-like carbon, that is carbon atoms not attached to hydrogen and $E_{\rm CH}/k$ (=946 K) is the fitted energy per benzene-like carbon and its adjoining H-atom. Graphene-like carbons are C-atoms with three covalent bonds with carbons, whereas benzene-like carbon have two covalent bonds with carbons and one bond with a hydrogen atom. Graphenes are PAHs where all the hydrogens have been stripped away. The value for $E_{\rm CC}/k$ is consistent with the measured range of adsorption energies of graphene on amorphous SiO_2, which lies between 450 and 1685 K per carbon (Thrower et al. 2013; Kumar et al. 2016). The adsorption energies are also consistent with the theoretical values of Mészár et al. (2013).

The fitting formula is valid for PAH made of up to 100 carbon atoms. For bigger PAHs, the formula gives values that are larger than the heat of vaporization of graphite of $\Delta H_{\rm f}/k = 86\,240$ K, Fig. A.4 (Pierson 1993). For circumcoronene, the estimated desorption energy is 34 380 K. A simple way to estimate the condensation temperature $T_{\rm cond}$ is to balance the adsorption with the thermal desorption

$$\sigma_{\rm dust} n_{\rm dust} n_{\rm PAH} S_{\rm PAH} \sqrt{\frac{8kT_{\rm cond}}{\pi m_{\rm PAH}}} = n_{\rm PAH\#} \nu_{\rm osc} \exp\left(-E_{\rm des}/kT_{\rm cond}\right), \tag{A.26}$$

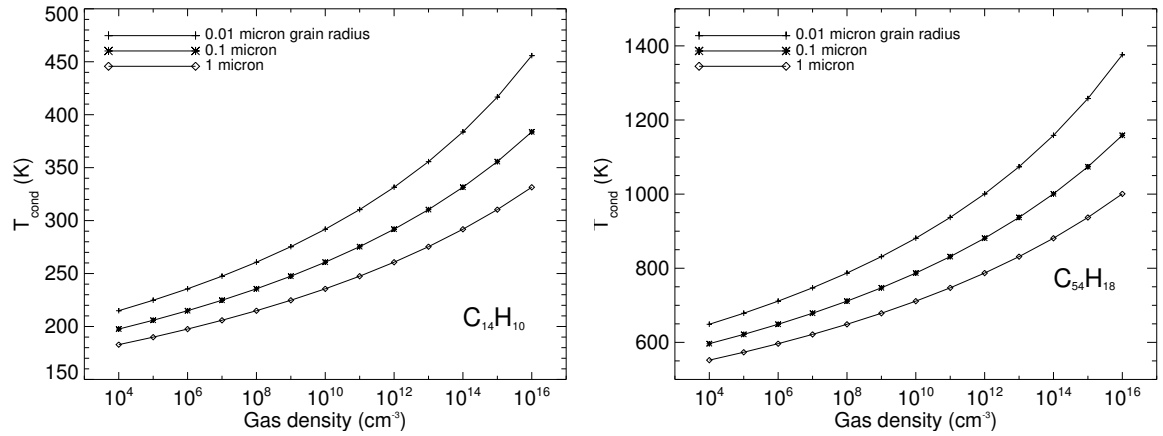

Fig. A.2. PAH condensation temperature for anthracene ($C_{14}H_{10}$) and circumcoronene ($C_{54}H_{18}$) assuming three different grain radii.

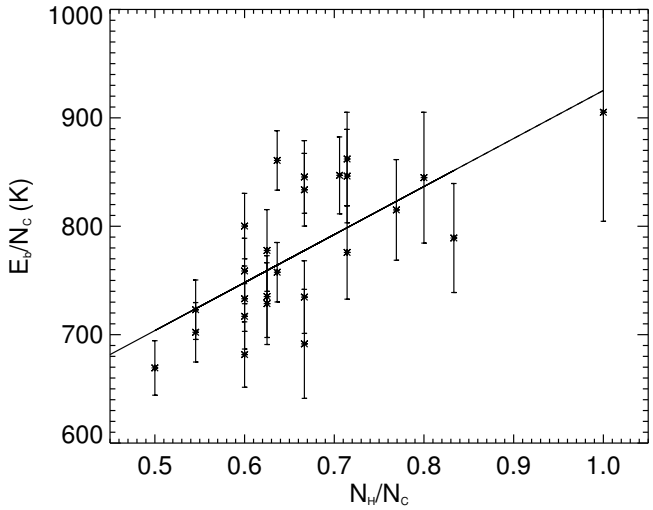

Fig. A.3. PAH binding energy normalized to the number of carbon atoms.

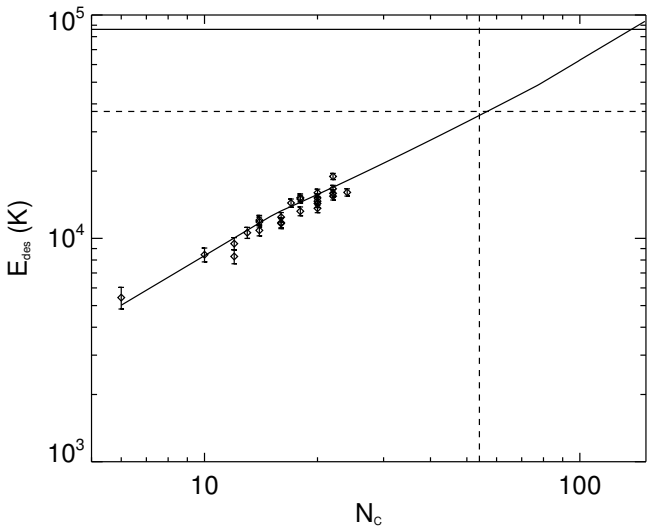

Fig. A.4. PAH desorption energy. The horizontal line corresponds to the limit imposed by the heat of vaporisation of graphite. The dashed-lines designate the desorption energy for circumcorene ($N_C = 54$).

where the exponential prefactor is (Aikawa et al. 1996)

$$\nu_{\rm osc} = \sqrt{\frac{2 n_{\rm surf} E_{\rm des}}{\pi^2 m_{\rm PAH}}} \ {\rm s}^{-1}. \tag{A.27}$$

$S_{\rm PAH}$ is the sticking coefficient for PAH molecules and $n_{\rm PAH}$ and $n_{\rm PAH\#}$ are the number density of PAH in the gas phase and adsorbed on surfaces respectively. The number of surface adsorption sites is assumed to be $n_{\rm surf} = 1.5 \times 10^{15}$ cm^{-2} for grains with a radius of 0.1 μm. The average number of dust grains in the disk is

$$n_{\rm d} = \frac{2.2 \, {\rm amu} \, n_{\rm H}}{(4/3)\pi \rho_{\rm d} \langle a^3 \rangle \delta} \approx 2.907 \times 10^{-15} n_{\rm H} \left(\frac{\mu {\rm m}^3}{\langle a^3 \rangle} \right) \left(\frac{100}{\delta} \right), \tag{A.28}$$

where δ is the gas-to-dust mass ratio which is assumed to be 100. We have assumed a silicate mass density of 3.0 g cm^{-3}. The balance between adsorption and thermal desorption for a gas density of 10^{10} cm^{-3}, a grain radius of 1 μm, a gas-to-dust mass ratio of 100, and assuming $n_{\rm PAH} = n_{\rm PAH\#}$ and a sticking coefficient of unity, leads to a condensation temperature for circumcoronene of ~710 K. In disks, PAHs should stick onto silicate grains and to each other. The condensation temperature for anthracene and circumcoronene is shown in Fig. A.2. The desorption of PAHs occurs thermally, induced by cosmic ray hits on the grains, and by absorption of a UV photon. We assumed a yield of 10^{-3} per absorbed photon for the photodesorption and a standard cosmic-ray induced desorption similar to the other ice species. The encounter between two PAHs can also result in the formation of clusters, which may subsequently grow by further accretion of PAHs. However, this mechanism is not accounted for in our current model.

A.7. X-ray chemistry

The X-ray chemistry in ProDiMo is described in detail in the appendix of Meijerink et al. (2012). Abbreviations for the references are listed in Table A.1.

The individual atomic ionization cross sections are used to derive the molecular dissociation rate from the individual ionization rates using the relative weight difference. If the difference in atomic weight between the components of the molecule is large, the cross section of the heavier one is used. If the difference is small, the cross sections are combined (Aresu et al. 2011). An example is the reaction CO + XPHOT which can lead

to $C^{2+} + O$, $C^+ + O^+$, or $C + O^{2+}$, so that the total cross section is the sum

$$\sigma_{CO} = \frac{1}{3}\sigma_C + \frac{1}{6}(\sigma_C + \sigma_O) + \frac{1}{3}\sigma_O, \quad (A.29)$$

where σ_{El} is the ionization cross sections of the element, in this case C and O.

More detailed explanations and discussions of rates can be found in Ádámkovics et al. (2011). The di-electronic recombination rates are from tables of Landini & Fossi (1991), Badnell et al. (2003), Badnell (2006), Zatsarinny et al. (2003) and subsequent papers of this series. In case of X-rays, the high temperature di-electronic recombination rates get added to the radiative recombination rates taken from UMIST. The two elements Ne and Ar have only di-electronic recombination rates currently available. We include here also charge exchange reaction of Ar and Ne with water, O_2, CO, N_2, CH_4, NH_3, CO_2, and NO. In addition we consider charge exchange between He^+ and Ne.

Appendix B: How E_{ads} affects line fluxes

We show in Figs. B.1 to B.3 how models with different sets of adsorption energies (Aikawa, GH06, UMIST2012 and temperature-dependent E_{ads}) affect our selection of line fluxes.

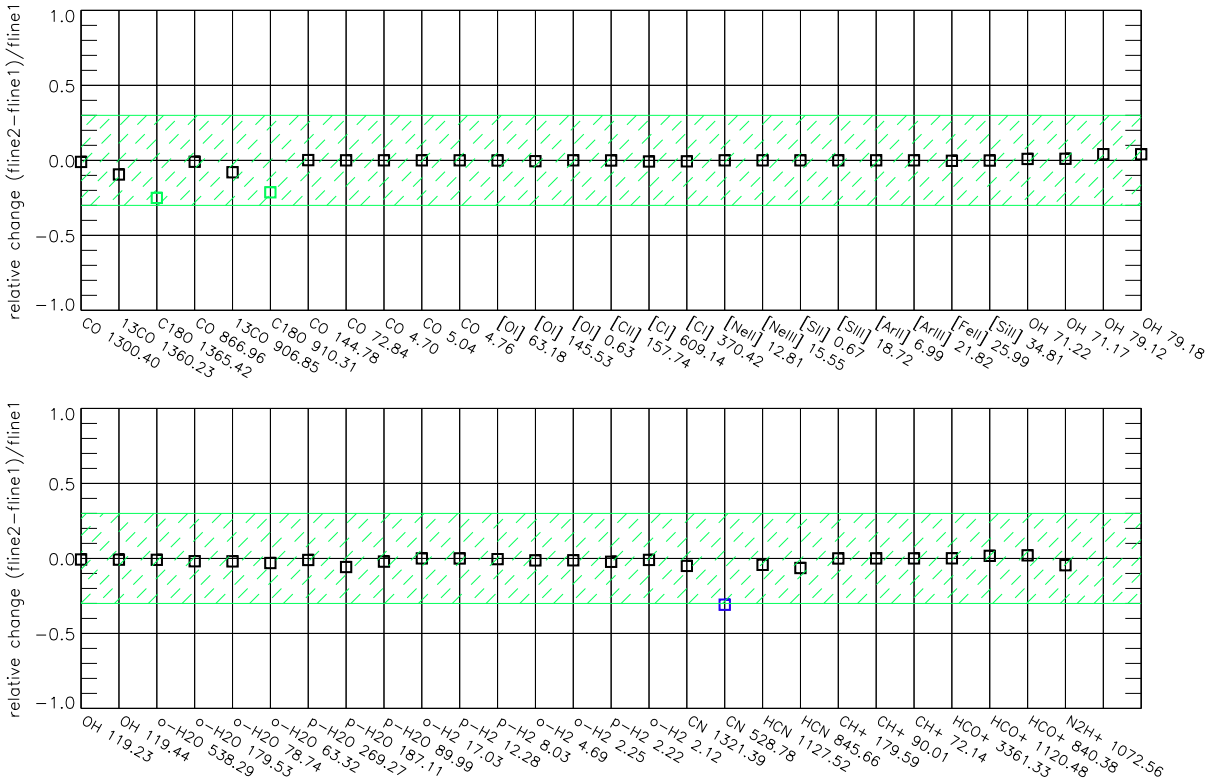

Fig. B.1. Comparison of line fluxes for two sets of adsorption energies: Aikawa (fline1, model 1) and GH06 (fline2, model 5). Black and green squares denote differences of less than 25% and less than a factor two respectively, blue squares and red triangles denote differences larger than a factor three and ten respectively.

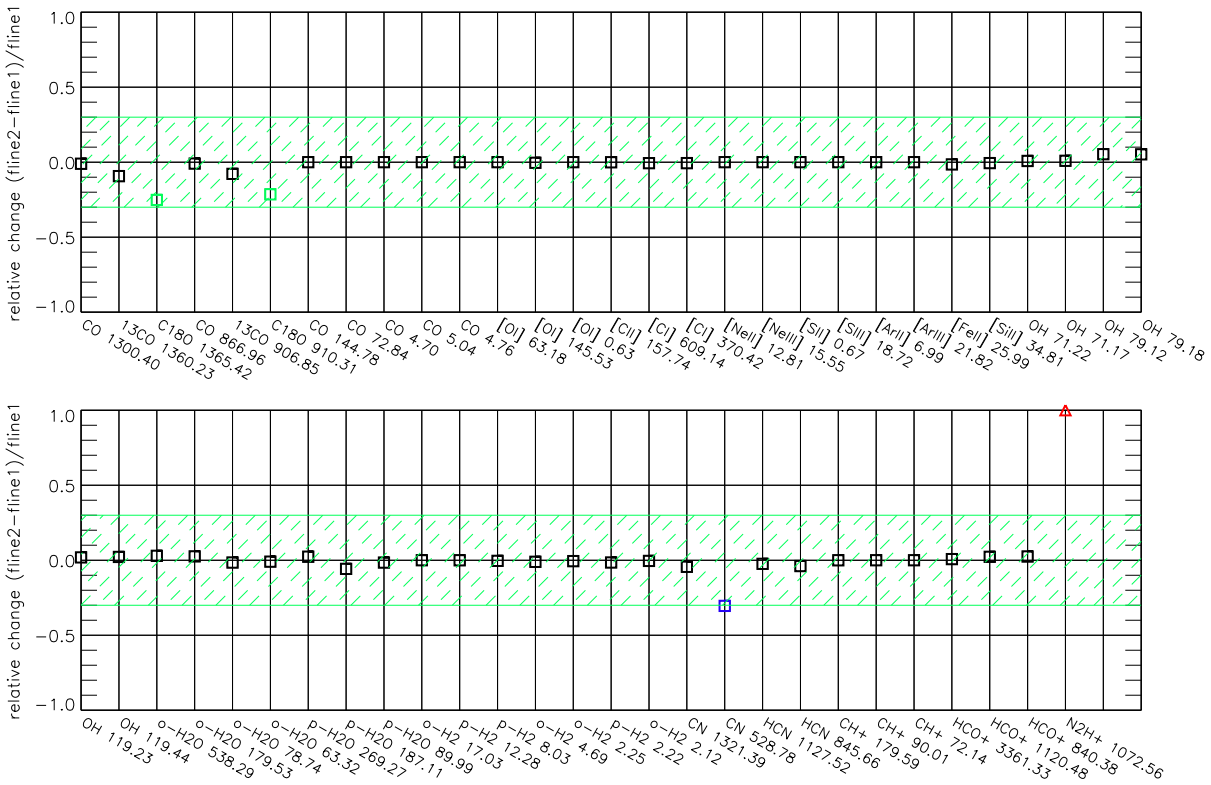

Fig. B.2. Comparison of line fluxes for two sets of adsorption energies: Aikawa (fline1, model 1) and UMIST2012 (fline2, model 6). Black and green squares denote differences of less than 25% and less than a factor two respectively, blue squares and red triangles denote differences larger than a factor three and ten respectively.

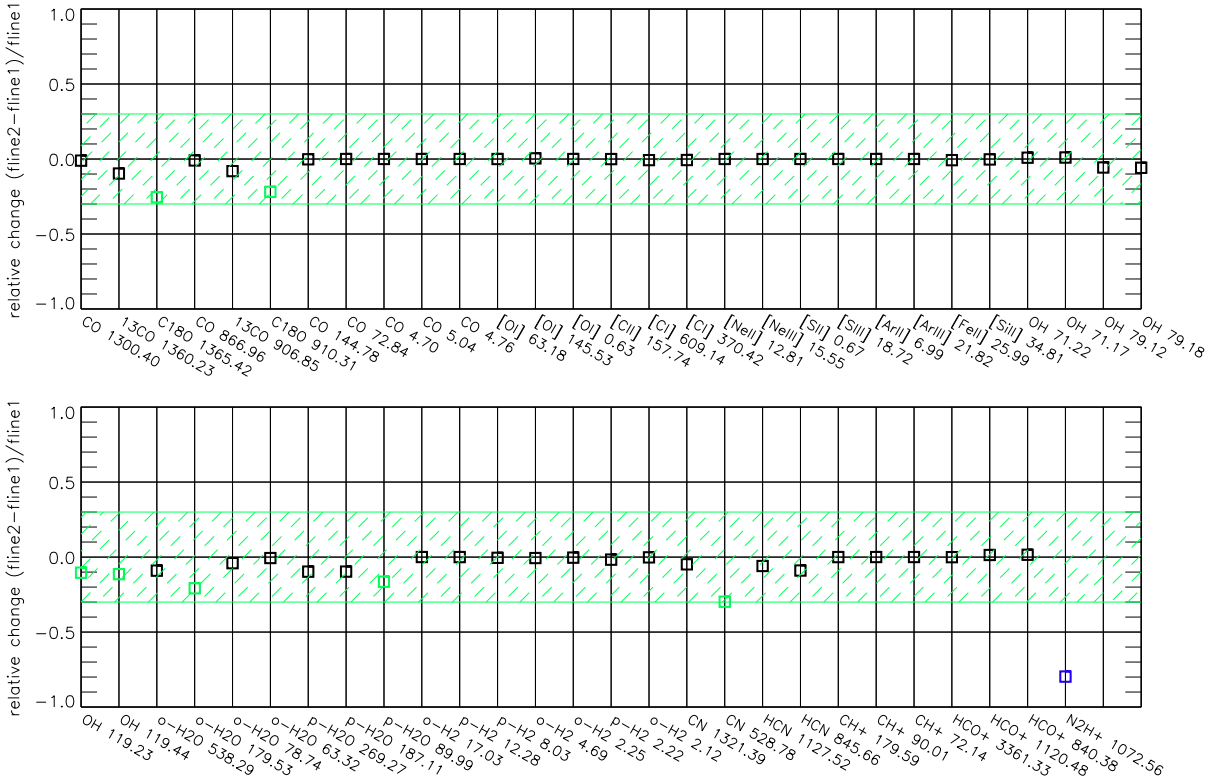

Fig. B.3. Comparison of line fluxes for two sets of adsorption energies: Aikawa (fline1, model 1) and T-dependent adsorption energies (fline2, model 7). Black and green squares denote differences of less than 25% and less than a factor two respectively, blue squares and red triangles denote differences larger than a factor three and ten respectively.